Strategies for numerical modeling the behavior of RC beams strengthened in shear using the ETS technique

M. Breveglieri [a,b,*], J.A.O. Barros [b], A. Aprile [a], A. Ventura-Gouveia [c]

[a] *ENDIF, Dep. of Eng., University of Ferrara, 44122 Ferrara, Italy*
[b] *ISISE, Dep. of Civil Eng., Univ. of Minho, Azurém, 4810-058 Guimarães, Portugal*
[c] *ISISE, Dep. of Civil Eng., Polytechnic Institute of Viseu, 3504-510 Viseu, Portugal*

ABSTRACT

The strategy to simulate the crack shear stress transfer in a fixed smeared crack model for concrete is crucial to correctly predict the deformational and cracking behavior of RC elements that exhibit shear failure. This work presents a shear softening law able to correctly simulate the shear stiffness degradation and stress transfer during the crack opening. In cracked concrete, the element of the matrix corresponding to the fracture mode II is represented here by a $\tau_t^{cr} - \gamma_t^{cr}$ diagram, describing the shear behavior of the ith crack. The predictive performance is evaluated simulating RC beams failing in shear strengthened using the Embedded Through-Section Technique. According to this technique holes are opened through the cross section, with the desired inclination, and steel or FRP bars are introduced into these holes and bonded to the concrete substrate with adhesive materials. The parameters influencing the shear softening law are analyzed through a parametric study, furthermore a simple rule to estimate these parameters is provided and its predictive performance is assessed. The presented approach represents a valid alternative to the shear retention function.

© 2016 Published by Elsevier Ltd.

1. Introduction

The evaluation of the predictive performance through the finite element method (FEM) of reinforced concrete (RC) elements failing in shear requires a material nonlinear constitutive model able to simulate the progressive shear stiffness degradation following concrete cracking. It has been demonstrated that, for a smeared crack approach that adopts the concept of fixed cracks or multidirectional fixed cracks [1,2], an appropriate simulation of the shear stress transfer is an essential requisite to accurately predict the load-deflection response up to ultimate load as well as the failure mode [3,4].

A widely used strategy to numerically simulate the shear stiffness degradation in fixed and multi-directional fixed smeared crack models consists in the introduction of a reduced shear modulus in the crack constitutive matrix after crack initiation, through the adoption of a shear retention parameter or function. In the past, a constant value was adopted for the shear retention factor, even though the uncertainty on the value to be adopted [5–7], as well as the incapacity of this approach in simulating the degradation of shear resisting mechanisms with the increase of the crack opening, leading to overestimations of the load carrying capacity and inconsistent crack pattern predictions; in an attempt of overcoming these deficiencies, later the shear retention parameter was assumed decreasing with the increase of the tensile strain normal to the crack plane [8–12]. This model

takes into account that friction resisting mechanisms, like aggregate interlock between the two surfaces of a crack, decrease with the increase of the crack opening. In spite of the better predictions ensured by this type of approach, the predictive performance in terms of load carrying and deflection capacity, as well as in respect the crack pattern, are still not good enough in structures failing in shear. In fact, in these conditions this approach overestimates the stiffness and the load carrying capacity when compared to the experimental results, and no clear shear failure is captured numerically. As a result of a large number of tests on the shear stress transfer across plain and reinforced concrete, analytical models able to describe this mechanical phenomenon in terms of local crack stress versus crack sliding relationship have been developed [13–18]. In general these semi-empirical models take into account several factors such as the maximum aggregate size, the strain normal to the crack plane, dilatancy effects and concrete compressive strength, and good agreement with experimental results was pointed out. The mentioned models were implemented in computational programs based on the FEM, by adopting a smeared crack approach for simulating the cracking process, where a characteristic length bridge the concept of crack width to the crack normal strain, as well as the crack sliding to the crack shear strain [3,18–23]. The definition of this characteristic length is still an open research topic. Vecchio [20], Dabbagh and Foster [19] and Pimentel et al. [22] proposed the crack spacing to bridge crack width and crack sliding with the corresponding crack normal and crack shear strain, but as demonstrated by Jahanmohammadi and Soltani [24], this approach is only applicable in concrete structures reinforced with smeared reinforcement, where relatively large number of smeared cracks is expected to be formed, and models of enough accuracy for predicting the crack spacing are available. For beams failing in shear,

* Corresponding author at: ENDIF, Dep. of Eng., University of Ferrara, 44122 Ferrara, Italy.

Email addresses: matteo.breveglieri@unife.it (M. Breveglieri); barros@civil.uminho.pt (J.A.O. Barros); alessandra.aprile@unife.it (A. Aprile); ventura@estgv.ipv.pt (A. Ventura-Gouveia)

characterized by deficient shear reinforcement, where relatively small number of shear dominant cracks are formed, these approaches are not recommended. Furthermore, the results from the simulations with these approaches are dependent of the mesh refinement due to the independence of the softening diagrams on a length representing the cracking dimension into the area/volume of the finite element.

In the attempt of capturing more accurately the behavior of RC elements failing in shear, Rots and de Borst [25] proposed a diagram for modeling the crack shear stress versus crack shear strain $\left(\tau_t^{cr} - \gamma_t^{cr}\right)$ of a bilinear nature, with a softening branch defined based on the crack shear strength and mode II fracture energy. For bridging the crack sliding with the crack shear strain these authors proposed the crack band width adopted for bridging the crack width with the crack normal strain. This approach was later extended to shell type structures and those simulated by solid finite elements by Ventura-Gouveia [26] by adopting a multi-directional fixed smeared crack model. However, no recommendations were proposed to determine the parameters defining the $\tau_t^{cr} - \gamma_t^{cr}$, which is a serious concern on the use of this approach, mainly when exploring new shear reinforcement and shear strengthening techniques. This paper aims to contribute for a better physical interpretation of the parameters defining the $\tau_t^{cr} - \gamma_t^{cr}$, the influence they have on the behavior of beams shear strengthened according to a new technique, and propose a methodology for estimating the values of the model parameters.

In this regards, the constitutive model is briefly described in this work, and a deep investigation of the parameters influencing the proposed model is carried out simulating experimental tests on RC beams shear strengthened according to the Embedded Through-Section (ETS) technique. This recent technique consists of opening holes throughout the height of the element's element cross section, with the desired inclinations; then steel or FRP bars are introduced into these holes and bonded to the concrete substrate with adhesive materials. Its effectiveness in upgrading shear resistance of reinforced concrete structures, has already been assessed and compared with other FRP-based strengthening techniques [27–31]. The experimental program is composed of RC-T cross section beams strengthened by using steel bars, and is characterized by different internal shear reinforcement, percentage and inclination of the strengthening ETS bars.

2. Numerical model

In a previous work a total crack shear stress-shear strain approach with the aim to numerically reproduce the decrease of shear stress transfers with the increase of the crack sliding and crack opening was implemented for a better simulation of the strengthened beams failing in shear and in flexural/shear [32]. In concrete structures failing in bending, and those failing in tension-shear (where crack width propagation is much more dominant than crack sliding), this strategy leads to simulations with reasonable accuracy. The most important aspect introduced in the model presented here is the treatment of the concrete fracture mode II by using a softening diagram to simulate the crack shear stress vs. crack shear strain $\left(\tau_t^{cr} - \gamma_t^{cr}\right)$ [25]. The presented model is capable of great accuracy in simulating the RC beams failing in shear [33,34]. This enhancement of the constitutive model allows an approximate measurement of the maximum carrying capacity, deformational response, and crack pattern of RC beams failing in shear.

In the following sections, a brief description of the formulation of the multi-directional fixed smeared crack model is presented and the crack shear stress vs. crack shear strain softening diagram described. The model is implemented in FEMIX, a FEM-based computer program [35].

2.1. Multi-directional fixed smeared crack model

At the domain of an integration point (IP) of a plane stress finite element and for the case of cracked concrete, the constitutive law is defined by the following equation:

$$\Delta\underline{\sigma} = \underline{D}^{crco}\Delta\underline{\varepsilon} \tag{1}$$

being $\Delta\underline{\sigma}$ and $\Delta\underline{\varepsilon}$ the vectors of the incremental stress and incremental strain components. In Eq. (1), $\underline{D}^{crco}$ is the cracked concrete constitutive matrix, obtained by the following equation [12]:

$$\underline{D}^{crco} = \underline{D}^{co} - \underline{D}^{co}\left[\underline{T}^{cr}\right]^T \left(\underline{D}^{cr} + \underline{T}^{cr}\underline{D}^{co}\left[\underline{T}^{cr}\right]^T\right)^{-1}\underline{T}^{cr}\underline{D}^{co} \tag{2}$$

where $\underline{D}^{co}$ is the constitutive matrix for concrete between cracks, assumed with a linear elastic behavior, $\underline{T}^{cr}$ is the matrix that transforms the stress components from the coordinate system of the finite element to the local crack coordinate system, and $\underline{D}^{cr}$ is the crack constitutive matrix:

$$\underline{D}^{cr} = \begin{bmatrix} D_I^{cr} & 0 \\ 0 & D_{II}^{cr} \end{bmatrix} \tag{3}$$

where D_I^{cr} and D_{II}^{cr} are the constitutive softening/hardening modulus corresponding to crack opening mode I (tensile) and crack sliding mode II (shear), respectively. The behavior of non-completely closed cracks formed in an IP is governed by the following relationship:

$$\Delta\underline{\sigma}_\ell^{cr} = \underline{D}^{cr}\Delta\underline{\varepsilon}_\ell^{cr} \tag{4}$$

being $\Delta\underline{\sigma}_\ell^{cr}$ and $\Delta\underline{\varepsilon}_\ell^{cr}$, respectively, the local vector of the incremental crack stress components and the local vector of the correspondent incremental crack strain components in the coordinate system of the crack.

A simple Rankine criterion is used to detect crack initiation. When the maximum principal tensile stress exceeds the tensile strength at an IP of a finite element, the material contained in its influence volume changes from an uncracked to a cracked state. The crack propagation is mainly controlled by the shape of the tensile-softening diagram represented in Fig. 1 and the material fracture energy (Mode I). The trilinear diagram is defined by the normalized stress, α_i, and strain, ξ_i, parameters that represent the transitions points between the linear segments of this diagram. The ultimate crack strain, $\varepsilon_{n,u}^{cr}$, is defined as a function of the parameters α_i and ξ_i, fracture energy, G_f^I, tensile strength, $f_{ct} = \sigma_{n,1}^{cr}$, and crack band width, l_b, as follows [12,36];

$$\varepsilon_{n,u}^{cr} = \frac{2}{\xi_1 + \alpha_1\xi_2 - \alpha_2\xi_1 + \alpha_2}\frac{G_f^I}{f_{ct}l_b} \tag{5}$$

The fracture Mode II modulus, D_{II}^{cr}, as was originally proposed by [10], is obtained from:
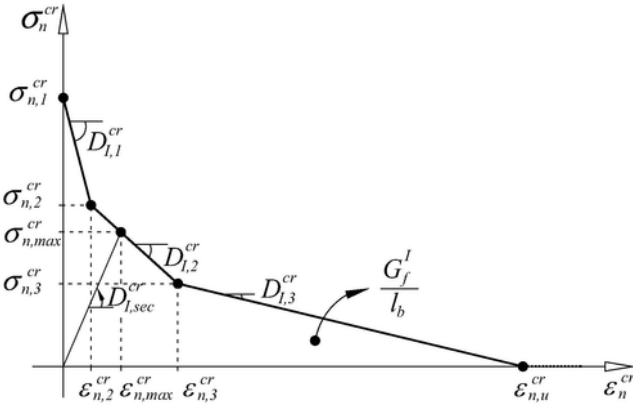
Fig. 1. Trilinear stress-strain diagram to simulate the fracture mode I crack propagation $\left(\sigma_{n,2}^{cr} = \alpha_1 \sigma_{n,1}^{cr}, \sigma_{n,3}^{cr} = \alpha_2 \sigma_{n,1}^{cr}, \varepsilon_{n,2}^{cr} = \xi_1 \varepsilon_{n,u}^{cr}, \varepsilon_{n,3}^{cr} = \xi_2 \varepsilon_{n,u}^{cr}\right)$.

$$D_{II}^{cr} = \frac{\beta}{1-\beta} G_c \qquad (6)$$

where β is the shear retention factor/function and G_c the concrete elastic shear modulus. For defining the β parameter Rots [10] recommended the adoption of a constant value or the following function:

$$\beta = \left(1 - \frac{\varepsilon_n^{cr}}{\varepsilon_{n,u}^{cr}}\right)^{p_1} \qquad (7)$$

where ε_n^{cr} and $\varepsilon_{n,u}^{cr}$ are, respectively, the actual and the ultimate crack normal strain, while p_1 can be 1–3 in order to simulate different decrease level of β with the increase of ε_n^{cr} [12].

Although, the description of the model is made using the formation of one crack in an IP, the multi-directional fixed smeared crack model implemented in the FEMIX computer program is capable of simulating the formation of multi-cracks in each IP [12,26].

2.2. Shear-softening diagram

The use of softening diagrams to reproduce the fracture mode I process is common in smeared and discrete crack models, but the use of softening diagrams to model the shear stress transfer across the crack is less usual. As described in the previous section, to simulate the fracture mode II process a shear retention factor is often used [10]. According to this approach, the shear stress transfer between the crack planes decreases with the increase of the normal crack strain (see Eq. (7)). In most structures, this strategy leads to simulations with enough accuracy. Exceptions can occur in structures that fail by the formation of a critical shear crack, where the adoption of a softening crack shear stress vs. crack shear strain relationship was originally demonstrated by Rots and de Borst [25] as capable of simulating more accurately the behavior of this type of structures. The crack shear softening diagram proposed by these authors is represented in Fig. 2, and its applicability was latter later extended to shell type structures and those simulated by solid finite elements by Ventura-Gouveia [26]. In this section a softening diagram to simulate the crack shear stress strain behavior is described. The crack shear dia-
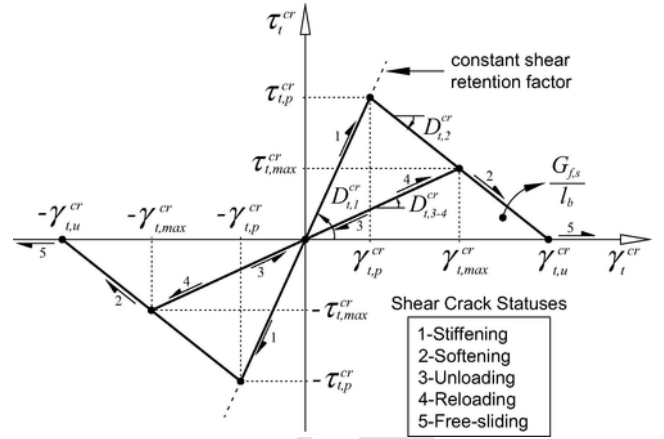
Fig. 2. Diagram to simulate the relationship between the crack shear stress and crack shear strain component $\left(\tau_t^{cr} - \gamma_t^{cr}\right)$ – shear softening law – and possible shear crack statuses.

gram, as previously introduced by [10,25] is represented in Fig. 2. The shear softening diagram starts at the origin because, according to the crack initiation criterion, when a crack initiates the crack shear stress is null. As a consequence of the rotation of the directions of principal stresses, shear stresses can develop across the surfaces of the crack [25]. The crack shear stress increases linearly until the crack shear strength is reached (first branch of the shear crack diagram), followed by a decrease in the shear residual strength (softening branch). The diagram represented in Fig. 2 is defined by the following expressions. Here the positive part of the diagram is explained while the negative part behaves in an equal way.

$$\tau_t^{cr}\left(\gamma_t^{cr}\right) = \begin{cases} D_{t,1}\gamma_t^{cr} & 0 < \gamma_t^{cr} \leqslant \gamma_{t,p}^{cr} \\ \tau_{t,p}^{cr} - \frac{\tau_{t,p}^{cr}}{\left(\gamma_{t,u}^{cr} - \gamma_{t,p}^{cr}\right)}\left(\gamma_t^{cr} - \gamma_{t,p}^{cr}\right) & \gamma_{t,p}^{cr} < \gamma_t^{cr} \leqslant \gamma_{t,u}^{cr} \\ 0 & \gamma_t^{cr} > \gamma_{t,u}^{cr} \end{cases} \qquad (8)$$

The shear fracture modulus, $D_{t,1}^{cr}$ is defined by Eq. (6), being D_{II}^{cr} replaced by $D_{t,1}^{cr}$, with the shear retention factor, β assuming a constant value in the range]0, 1[. Eq. (7) for defining β is only used as an alternative to the shear softening approach adopted in the present model. The peak crack shear strain, $\gamma_{t,p}^{cr}$ is obtained by the following equation:

$$\gamma_{t,p}^{cr} = \frac{\tau_{t,p}^{cr}}{D_{t,1}^{cr}} \qquad (9)$$

being, $\tau_{t,p}^{cr}$, the crack shear strength acquired from the input data.

The ultimate crack shear strain, $\gamma_{t,u}^{cr}$ is obtained by Eq. (9) and depends on the crack shear strength, $\tau_{t,p}^{cr}$, on the shear fracture energy (mode II fracture energy), $G_{f,s}$ and on the crack bandwidth, l_b as follows:

$$\gamma_{t,u}^{cr} = \frac{2G_{f,s}}{\tau_{t,p}^{cr} l_b} \qquad (10)$$

It is assumed in the present approach that the crack bandwidth, used to assure that the results are independent of the mesh refinement, can also be used to define the dissipated energy in the mode II fracture process. This strategy was already proposed by Rots and de Borst [25], and later also adopted by An et al. [18], where the same crack band width, related to a characteristic of the finite element, is taken for adjusting the softening modulus for both fracture modes (I and II). This strategy assumes that fracture energy mode I and II are properties of the material, being dissipated during the fracture process, where the capacity of the smeared cracks to transfer normal and shear stresses is automatically adjusted according to the mesh refinement adopted. Specific research on this topic is, however, recommended to be executed, but this is out-of-the-scope of the present work.

As a consequence of the formation of new cracks in the vicinity of existing ones, the existent cracks can close or reopen. The model must take into account this change of crack status. Indeed it does consider this with regard to the opening mode I and a similar approach is used for the crack shear component [12]. So, five shear crack statuses are proposed and their meaning is schematically represented in Fig. 2. Detailed information on how the model treats the crack statuses for both fracture modes is available in Ventura-Gouveia [26].

As shown in Fig. 2 the evaluation of the fracture mode II softening modulus D_{II}^{cr} of Eq. (3), depends on the branches defining the diagram. The crack mode II modulus of the first linear branch of the diagram is defined by Eq. (6), the second linear softening branch is defined by

$$D_{II}^{cr} = D_{t,2}^{cr} = -\frac{\tau_{t,p}^{cr}}{\gamma_{t,u}^{cr} - \gamma_{t,p}^{cr}} \qquad (11)$$

and the crack shear modulus of the unloading and reloading branches is obtained from

$$D_{II}^{cr} = D_{t,3"-"4}^{cr} = \frac{\tau_{t,max}^{cr}}{\gamma_{t,max}^{cr}} \qquad (12)$$

being $\gamma_{t,max}^{cr}$ and $\tau_{t,max}^{cr}$ the maximum crack shear strain already attained and the corresponding crack shear stress determined from the softening linear branch. Both components are stored to define the unloading/reloading branch (see Fig. 2).In free-sliding status, $|\gamma_t^{cr}| > |\gamma_{t,u}^{cr}|$ the crack mode II stiffness modulus, $D_{II}^{cr} = D_{t,5}^{cr}$ is null. To avoid numerical instabilities in the calculation of the stiffness matrix, when the crack shear status is "free-sliding" a residual crack shear stress value is assumed for this phase of sliding. A free-sliding status is also assigned to the shear crack status when $\varepsilon_n^{cr} > \varepsilon_{n,u}^{cr}$.

The crack shear stress vs. shear strain diagram represented in Fig. 2 was adopted in the simulations performed in the present work, but other more sophisticated diagrams were also implemented in the FEMIX computer program, and their corresponding formulations can be found elsewhere [26]. The accuracy of the model was already demonstrated for NSM CFRP shear strengthened beams [34].

3. Predictive performance of the numerical model

3.1. Experimental program

The predictive performance of the presented model is assessed using the experimental tests carried out by Breveglieri et al. [30,31] on T-cross section reinforced concrete (RC) beams shear strengthened according to the Embedded Through-Section (ETS) technique. The experimental program is composed by fifteen T cross section beams divided in three Series (Series 0S, 2S, 4S). Fig. 3 presents the geometry and the reinforcement details of the tested series. The reinforcement system was designed, using a high percentage of longitudinal reinforcement ($\rho_{sl} = 2.79\%$) in order to force the occurrence of a shear failure mode for all the beams of the experimental program. To localize shear failure in one of the beam's shear spans, a three-point load configuration was selected, with a different length of the beam's shear spans. The monitored beam span ($L_1 = 0.9$ m) is 2.5 times the effective depth of the beam's cross section ($L_1/d = 2.5$). The maximum shear force applied in the L_1 beam's span is calculated as $V_t = 0.6F_{max}$. Fig. 4 shows the different shear reinforcement systems applied in the L_1 beam's span of the tested beams; 0S-Series does not have conventional steel stirrups; 2S-Series has steel stirrups $\phi6@300$ mm, corresponding to a shear reinforcement ratio $\rho_{sw} = 0.10\%$ and 4S-Series has steel stirrups $\phi6@180$ mm, corresponding to a shear reinforcement ratio $\rho_{sw} = 0.17\%$.

3.1.1. Strengthening geometry and material characterization

Table 1 indicates the designation adopted for each beam and the strengthening configurations, namely, the number of applied ETS bars, inclination, spacing, shear strengthening ratio (ρ_{fw}), as well as the percentage of steel stirrups (ρ_{sw}) and total shear reinforcement ($\rho_{sw} + \rho_{fw}$). Each series has a reference beam without any strengthening system, and four beams with different ETS strengthening configurations, as an example the four strengthening configurations (beams 0S-S300-90, 2S-S300-45, 4S-S180-90 and 4S-S180-45) are represented in Fig. 4. The investigated parameters were the shear strengthening ratio (ρ_{fw}) and the inclination θ_f (90°, 45°) of the ETS bars, as well as the influence of the percentage of existing steel stirrups. The diameter of the ETS steel bars was 10 mm. The ETS strengthening ratio varied between 0.15% (ETS vertical bars spaced at 300 mm) and 0.34% (ETS bars at 45° and spaced at 180 mm). The average compressive strength (f_{cm}) was equal to 29.7 and 32.3 MPa, for 0S-
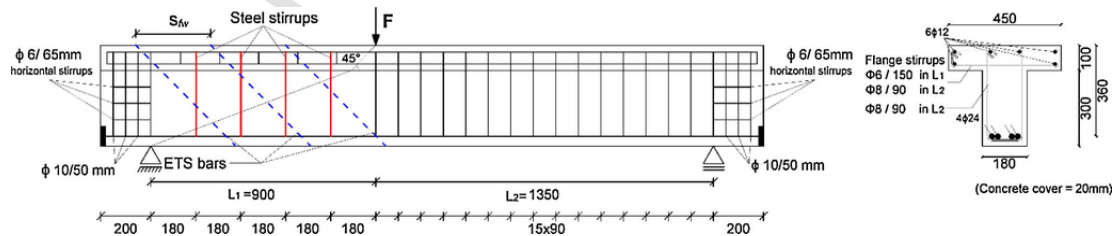

Fig. 3. Tested beams: geometry, steel reinforcements applied in all beams. Beam 4S-S300-45 is presented: stirrups spaced at 180 mm and inclined ETS bars spaced at 300 mm (all dimensions in mm).
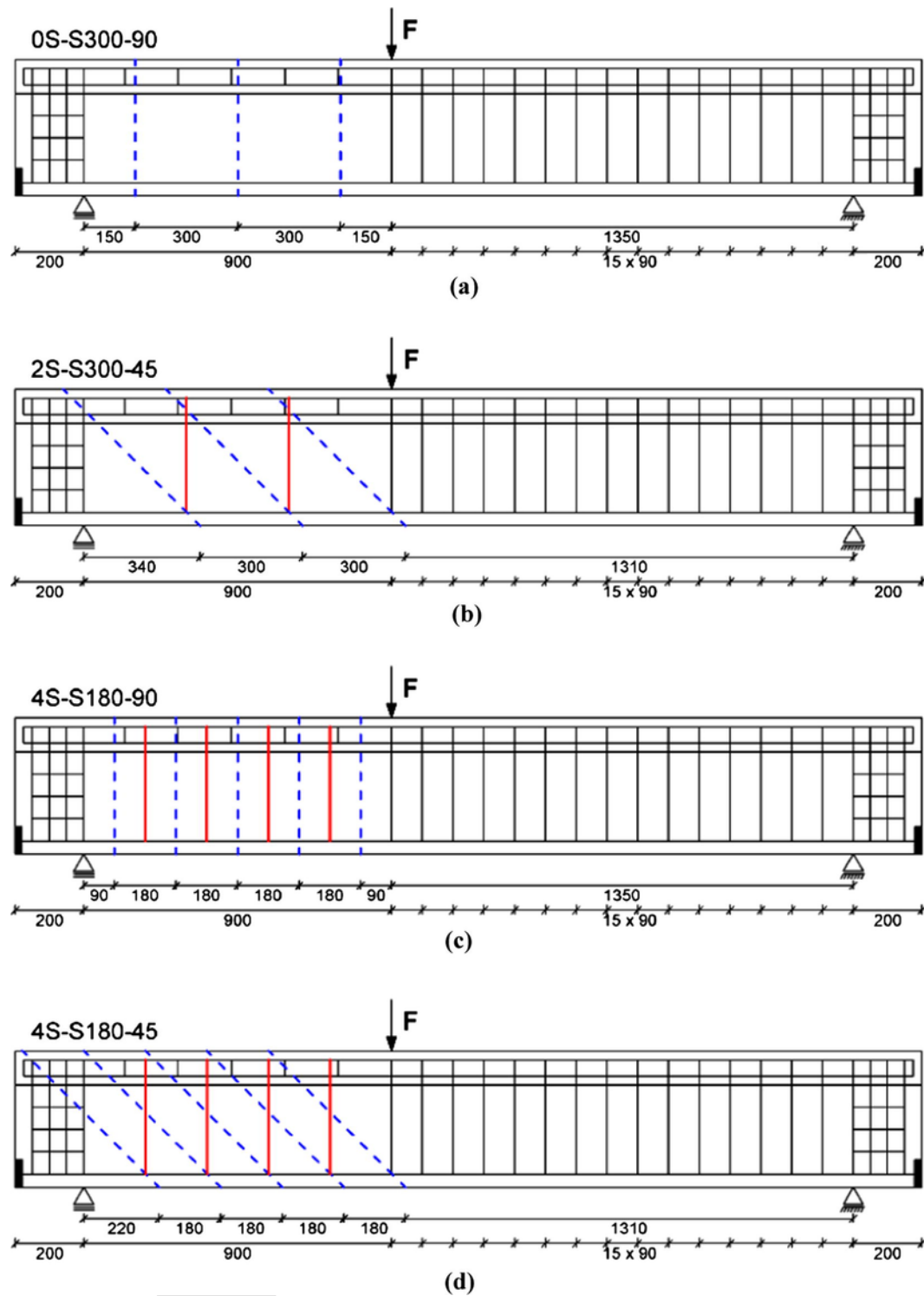
Fig. 4. Tested strengthening arrangement: (a) 0S-S300-90, vertical ETS spaced at 300 mm; (b) 2S-S300-45, inclined ETS spaced at 300 mm, (c) 4S-S180-90, vertical ETS spaced at 180 mm, (d) 4S-S180-45, inclined ETS spaced at 180 mm.

Series and 2S-Series and for 4S-Series, respectively. The maximum aggregate size was 16 mm. For the internal reinforcement high bond steel bars of 6, 10, 8, 12, and 24 mm diameter were used of a representative average yield stress and tensile strength of 550 MPa ($\varepsilon_{sy} = 275\%$) and 645 MPa, respectively. The adopted ETS steel bars were of the same class of the bars used for the flexural reinforcement and steel stirrups applied in the beams. Sikadur 32 N epoxy based adhesive of average tensile strength and an elasticity modulus, 20.7 MPa and 3.27 GPa, respectively, was used to bond the ETS steel bars to the concrete substrate The strain variations in steel stirrups and ETS bars, were monitored using electrical strain gauges (SGs).

Table 1
ETS shear strengthening configurations of the tested beams.

Number of bars	Angle [β]	ETS bar spacing [s_{fw}]	ETS Reinforcing ratio [ρ_{fw}]	0S-Ref		2S-Ref		4S-Ref	
n_{ETS}	[°]	[mm]	[%]^a	($\rho_{sw} = 0.0\%$)^b	$\rho_{sw} + \rho_{fw}$ [%]	($\rho_{sw} = 0.10\%$)^b	$\rho_{sw} + \rho_{fw}$ [%]	($\rho_{sw} = 0.17\%$)^b	$\rho_{sw} + \rho_{fw}$ [%]
3	90	300	0.15	0S-S300-90	0.15	2S-S300-90	0.25	4S-S300-90	0.32
3	45	300	0.21	0S-S300-45	0.21	2S-S300-45	0.31	4S-S300-45	0.38
5	90	180	0.24	0S-S180-90	0.24	2S-S180-90	0.34	4S-S180-90	0.41
5	45	180	0.34	0S-S180-45	0.34	2S-S180-45	0.44	4S-S180-45	0.51

^{a} The ETS percentage was obtained from $\rho_{fw} = (A_{fw}/(b_w \cdot s_{fw} \cdot \sin \theta_f)) \times 100$ where A_{fw} is the area of the ETS bar cross section.

^{b} The percentage of the vertical steel stirrups was obtained from $\rho_{sw} = (A_{sw}/(b_w \cdot s_{sw})) \times 100$ where A_{sw} is the cross sectional area of the arms of a steel stirrup, and s_{sw} is the spacing of the stirrups.

3.1.2. Main experimental results

The load (F)-deflection (u_L) diagram for the tested series is presented Fig. 5. The main results of the experimental tests are presented in Table 2, where F_{max} is the maximum load attained by the beams and u_{Lmax} is the displacement in the loaded section at F_{max}. The strengthening efficiency of the ETS technique can be evaluated by considering the $\Delta F/F_{max,Ref}$ ratio, where $F_{max,Ref}$ is the maximum load of the reference beam, and $\Delta F = F_{max} - F_{max,Ref}$ is the increase of maximum load provided by each ETS arrangement. All the tested beams presented significant increment of load carrying capacity with the exception of 4S-S300-90 for the reason explained in [31,37]. The deflection capacity was also improved by the ETS strengthening.

All the tested beams showed similar behavior up to the formation of the first diagonal crack, that formed at an approximate load of 113 kN ($u_L = 0.98$ mm), 100 kN ($u_L = 0.91$ mm) and 135 kN ($u_L = 1.37$ mm) in case of the reference beams 0S-Ref, 2S-Ref and 4S-Ref, respectively. The ETS steel bars offered resistance to crack opening and sliding, bridging the shear cracks, enhancing concrete's contribution to the shear resistance due to the aggregate interlock effect. The latter led to a higher load carrying capacity after shear crack initiation, and higher stiffness retention in comparison to the unstrengthened beams. All the beams exhibited a shear failure mode, since a quite high flexural reinforcement was adopted in order to avoid flexural failure mode.

0S-Series, characterized by the absence of stirrups in the strengthened shear span ($\rho_{sw} = 0.0\%$), presented the highest strengthening efficiency amongst the tested series, with an increase of load carrying capacity that ranged from 40% to 136%. For the ETS vertical bars, the beams with the lowest percentage of ETS bars, $\rho_{fw} = 0.15\%$ (0S-S300-90), and with the highest $\rho_{fw} = 0.24\%$ (0S-S180-90) presented an increase of load carrying capacity of 39.5% and 64.6%, respectively. The highest increase of load carrying capacity was obtained in the beams with ETS bars inclined at 45°. In fact for the beams 0S-

S300-45 ($\rho_{fw} = 0.24\%$) and 0S-S180-45 ($\rho_{fw} = 0.34\%$) the load carrying capacity increased 123.4% and 136.3%, respectively. 2S-Series (Fig. 3) was shear reinforced with 2-arms φ6 mm steel stirrups @300 mm ($\rho_{sw} = 0.10\%$). For the ETS vertical bars, the beams with the lowest percentage of ETS bars, $\rho_{fw} = 0.15\%$ (2S-S300-90), and with the highest percentage, $\rho_{fw} = 0.24\%$ (2S-S180-90), presented an increase of load carrying capacity of 30.4% and 68.1% respectively. As for the 0S-Series, in the 2S-Series the highest strengthening effectiveness was obtained in beams with ETS bars inclined at 45°. The beams 2S-S300-45 ($\rho_{fw} = 0.21\%$) and 2S-S180-45 ($\rho_{fw} = 0.34\%$) presented an increase in the load carrying capacity of 68.2% and 108.5%, respectively. 4S-series was shear reinforced with 2-arms φ6 mm existing steel stirrups @180 mm ($\rho_{sw} = 0.17\%$). For the ETS vertical bars, the beams with the lowest percentage of ETS bars, 4S-S300-90 ($\rho_{fw} = 0.15\%$), and 4S-S180-90 ($\rho_{fw} = 0.24\%$), presented the lowest increase of load carrying capacity of 4.8% and 16.8%, respectively, demonstrating the influence of the percentage of existing steel reinforcement ratio. In the beams with ETS bar inclined at 45°, a significative increase of load carrying capacity was obtained; beams 4S-S300-45 ($\rho_{fw} = 0.21\%$) and 4S-S180-45 ($\rho_{fw} = 0.34\%$) presented an increase of load carrying capacity of 56.1% and 60.1%, respectively.

The ETS shear strengthening systems failed by the debond at the bar/adhesive interface; however due to the ETS bars' higher confinement provided by the surrounding concrete, the bond performance was able to mobilize the yield stress of the steel bars. Steel yielding in ETS bars, as well as in stirrups, was also observed in the highest percentage of strengthening. During this type of crack's opening and sliding process, the vertical and inclined ETS bars that cross them underwent axial and transversal forces, causing the ETS bars to scratch the surrounding epoxy adhesive.

The recorded strain values [30,31] showed that high strains have been generally recorded in inclined ETS, and in vertical bars crossed by the critical shear crack at half of the beam's height (Beam 0S-S180-90), thus demonstrating the importance of the available bond
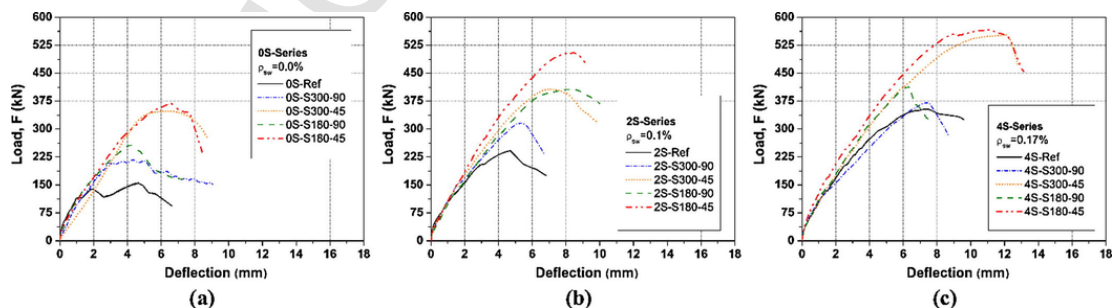

Fig. 5. Force vs deflection at the loaded section for (a) 0S-Series, (b) 2S-Series, (c) 4S-Series.

Table 2
Experimental results of 0S-Series, 2S-Series and 4S-Series.

	$F_{\max}$ [kN]	$u_{L\max}$ [mm]	$\Delta F / F_{\max,Ref}$ [%]
0S-Ref	156.1	4.66	–
0S-S300-90	217.8	4.37	39.5
0S-S300-45	348.6		123.4
0S-S180-90	256.8	4.31	64.6
0S-S180-45	368.8	6.56	136.3
2S-Ref	242.1	4.70	–
2S-S300-90	315.7	5.32	30.4
2S-S300-45	407.1	7.03	68.2
2S-S180-90	406.8	8.27	68.1
2S-S180-45	504.7	8.37	108.5
4S-Ref	353.8	7.35	–
4S-S300-90	370.9	7.43	4.8
4S-S300-45	552.4	12.03	56.1
4S-S180-90	413.2	6.32	16.8
4S-S180-45	566.4	11.01	60.1

Table 3
Values of the parameters of the concrete constitutive model used to simulate the tested beams.

Poisson's ratio (ν_c)	0.15
Initial Young's modulus (E_c)	30.7 N/mm²
Compressive strength (f_c)	29.7 N/mm²
Trilinear tension-softening diagram	$f_{ct} = 1.9$ N/mm², $G_f = 0.07$ N/mm
	$\xi_1 = 0.004$, $\alpha_1 = 0.3$, $\xi_2 = 0.05$, $\alpha_2 = 0.2$
Parameter defining the mode I fracture energy available to the new crack [11]	$p_2 = 2$
Crack bandwidth (l_b)	Square root of the area of Gauss integration point
Threshold angle	$\alpha_{th} = 30°$
Maximum number of cracks per integration point [11]	2
Ultimate crack shear sliding	MAXIMUM_CRACKWIDTH

length in the evaluation of the ETS bar contribution as already demonstrated for EBR and NSM techniques [38–41]. Steel stirrups showed similar results in terms of strain variation equal to the ETS bars, moreover, the attainment of yield strain was facilitated by the full anchorage at the top and bottom longitudinal reinforcement. Stirrups rupture in a small number of specimen (2S-S300-45, 4S-S180-90) was observed.

As already demonstrated in beams strengthened with the ETS [28,29], EBR and NSM techniques [42–45], the effectiveness of the ETS strengthening system decreases with the increase of the ρ_{sw} shear reinforcement ratio of existing steel stirrups. It has been shown in Breveglieri et al. [30,31] that the shear strengthening efficacy rises with the increase of $\rho_{sw} + \rho_{fw}$ and the most effective configuration is obtained by adopting inclined ETS bars. The higher shear effective-

ness showed by the ETS inclined bars can be justified by the orientation of the diagonal cracks that tends to be almost orthogonal to the ETS bars. Furthermore, for vertical ETS bars, the total resisting bond length of the ETS system is lower than the one for the inclined bars.

3.2. Finite element mesh, integration schemes and materials' constitutive law

In order to model the concrete part of the RC beams, all the numerical simulations used 8-noded serendipity plane stress (PSTE) finite elements, averaging a size of 25×25 mm. The longitudinal steel bars, stirrups and the ETS strengthening bars were modeled with 3-nodes embedded cable (EC) type elements (one degree of freedom per each node) that were assumed to be perfectly bonded to the surrounding concrete. A Gauss-Legendre integration scheme was adopted for both PSTE and EC elements, of 2×2 integration points (IP) in case of PSTE, and 2 IP for ECs. Two sets of smeared cracks were allowed to be formed at each integration point, according to a threshold angle of 30° for crack opening criterion [46]. A modified version of the Newton-Raphson method was adopted, i.e. the stiffness matrix of the structure in the iterations of a load increment is the one evaluated in the first iteration, $K_T^i = K_T^0$. The loading process was controlled by the arch length technique [47] by imposing an increment of vertical displacement in point P (Fig. 6) that varied between 0.1 and 0.3 mm, and an energy convergence criteria of 1.0‰ was adopted. An example of a finite element mesh used for the simulation of 4S-S180-45 beam is represented in Fig. 6. The values that define the concrete constitutive model discussed in Section 2 are indicated in Table 1. Since in RC beams failing in shear traction, the volume of concrete experiencing nonlinear deformation in compression is relatively small [34,48,49], the behavior of concrete in compression was assumed linear-elastic. The trilinear tension-softening diagram represented in Fig. 1 was adopted to simulate the concrete fracture mode I process. The value of the concrete tensile strength and fracture energy were obtained according to the Model Code recommendations [50].

For modeling the crack shear behavior, the $\tau_t^{cr} - \gamma_t^{cr}$ diagram represented in Fig. 2 was used, and its defining parameters' influence on the beams' response was investigated; this type of beams' load carrying and deflection capacity, as well as its crack pattern, are quite dependent on the values adopted for this crack shear softening diagram.

For assessing the values for the $\tau_t^{cr} - \gamma_t^{cr}$ of the concrete model of the tested beams $\left(\beta, \tau_{t,p}^{cr}, G_{f,s} \right)$, an inverse analysis was executed by fitting as much as possible, not only the load-versus-deflection and the load-versus-strain relationships registered experimentally, but also the crack pattern observed in the beams' failure stage. This inverse analysis generated interval of values obtained for β, $\tau_{t,p}^{cr}$ and
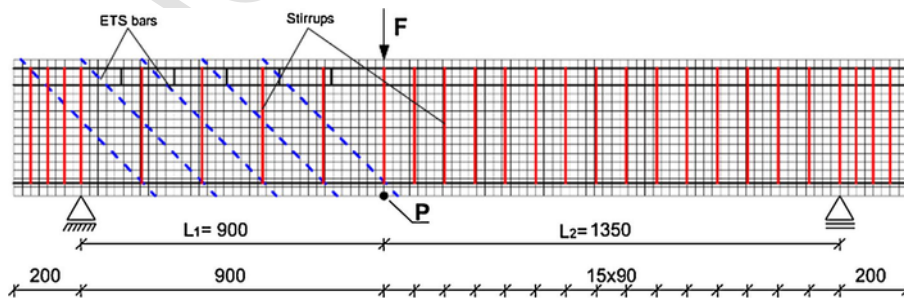
Fig. 6. Finite element mesh for beam 4S-S180-45 (dimensions are in mm).

$G_{f,s}$ that assured simulations of acceptable accuracy considering the results of the deflection response and crack pattern. These values are indicated in Table 4 along with the values that best fit (in bold) the behavior of the tested beams. The $\tau_{t,p}^{cr}$ can be assumed equal to 1.0 MPa, which corresponds to $0.10 f_{cm}^{2/3}$. This value is in agreement with those obtained by inverse analysis in previous studies [33,34,51,52], since they have ranged between $0.09 f_{cm}^{2/3}$ and $0.15 f_{cm}^{2/3}$ (average $\tau_{t,p}^{cr} = 0.12 f_{cm}^{2/3}$). The values obtained for the crack shear strength are quite close to the one obtained by Baghi and Barros [53] where specific research was conducted to derive the parameters of the crack shear softening diagram by performing Iosipescu shear tests and inverse analysis.

The almost independence of the results on the mesh refinement when using this type of model was already investigated by Edalat Behbahani et al. [54], mainly when a relatively refined mesh is used.

For modeling the behavior of the longitudinal steel bars, stirrups and ETS bars, both in tension and in compression, a trilinear stress-strain diagram was adopted (Fig. 7) [12]. This diagram is defined by the points PT1 = $(\varepsilon_{sy}, \sigma_{sy})$, PT2 = $(\varepsilon_{sh}, \sigma_{sh})$ and PT3 = $(\varepsilon_{su}, \sigma_{su})$, and a parameter p that defines the shape of the last branch of the diagram (Fig. 7). Unloading and reloading linear branches with slope $E_s = \sigma_{sy}/\varepsilon_{sy}$ are assumed in the present approach. The values for defining this diagram were obtained from tensile tests, and the resulting values are indicated in Table 5.

The perfect bond assumption between reinforcement and concrete is common in literature [19,20,49,52], and as also demonstrated in this work can be accepted for an ultimate state design level, in contrast to a serviceability limit state analysis or crack width evaluation, where a proper bond modeling is of fundamental importance. In terms of structural design, the parameters affecting the bond properties of the reinforcement as: stiffness and surface properties of the reinforcement, snubbing effect, group effect, thickness of the concrete cover, loading conditions and strain rate, are difficult to model with accuracy, especially for the stirrups. It was observed by Chen et al. [48] that by changing the bond modeling conditions, the crack pattern can undergo substantial change, affecting the strains in both steel and strengthening as well as the maximum load carrying capacity; this evidenced the difficulty of choosing a proper bond-slip model. Even though the adoption of an accurate bond model can improve the numerical analysis and reduce the mesh dependency, Jendele and Cervenka [55] noticed that if an adequate mesh size is adopted, the bond model has mainly a minor effect on the tension stiffening. In the presented simulation, the adoption of a user customizable trilinear tensile softening-diagram (Fig. 1) allows to consider in part the tension stiffening effect due to the longitudinal reinforcement. Moreover, the perfect bond assumption can be here supported by narrow flexural cracks observed during the experimental tests, which means neglectable slip in longitudinal bars up to maximum load.

3.3. Simulation and discussion

The load-deflection relationships obtained experimentally and numerically are compared in Fig. 8. The simulations were ended where no convergence was not possible to attain. However, the crack pattern installed in the last converged loading step was also used to confirm that this loading stage corresponds to the eminence of failure. In fact at this load stage the crack pattern included a critical shear failure crack composed by crack with status of "completely open", which means that it is no longer possible to transfer any type of stresses.

Table 4

Values β, $\tau_{t,p}^{cr}$, $G_{f,s}$ used in the performed numerical simulation. The values that reproduced with the highest accuracy the experimental response are highlighted in bold character, the minimum and maximum values of the parameters used in the simulations are also indicated.

	β [–]	$\tau_{t,p}^{cr}$ [MPa]	$G_{f,s}$ [N/mm]
0S-Ref	**0.175**	**1.00**	**0.07**
Min	0.150	0.85	0.07
Max	0.22	1.00	0.1
0S-S300-90	**0.15**	**1.00**	**0.08**
Min	0.141	0.85	0.07
Max	0.150	1	0.14
0S-S180-90	**0.144**	**1.00**	**0.1**
Min	0.1	1.00	0.1
Max	0.150	1.1	0.2
0S-S300-45	**0.10**	**1.00**	**0.50**
Min	0.03	0.85	0.14
Max	0.15	1	1.3
0S-S180-45	**0.10**	**1.00**	**0.2**
Min	0.064	1	0.1
Max	0.15	1	0.768
2-Ref	**0.15**	**1.00**	**0.08**
Min	0.05	0.85	0.08
Max	0.15	1.00	0.15
2S-S300-90	**0.12**	**1.00**	**0.12**
Min	0.10	1	0.12
Max	0.15	1	0.182
2S-S180-90	**0.1**	**1.00**	**0.18**
Min	0.10	1	0.14
Max	0.15	1.25	0.45
2S-S300-45	**0.075**	**1.00**	**0.6**
Min	0.03	0.85	0.14
Max	0.15	1.00	1.3
2S-S180-45	**0.017**	**1.00**	**1.00**
Min	0.017	1	0.89
Max	0.2	1.25	1.75
4S-Ref	**0.1**	**1.00**	**0.22**
Min	0.05	1.00	0.1
Max	0.15	1.25	0.25
4S-S300-90	**0.09**	**1.00**	**0.14**
Min	0.09	1.00	0.14
Max	1.15	1.0	0.213
4S-S180-90	**0.075**	**1.00**	**0.45**
Min	0.075	1.00	0.14
Max	0.15	1.50	0.50
4S-S300-45	**0.02**	**1.00**	**0.9**
Min	0.01	0.85	0.51
Max	0.07	1.75	2.0
4S-S180-45	**0.030**	**1.00**	**1.5**
Min	0.012	1	0.3
Max	0.200	3	2.5

The numerical curves (red[1] color and including circle markers) were obtained by using for the $\tau_t^{cr} - \gamma_t^{cr}$ diagram the values (in bold) indicated in Table 4. This figure also indicates each beam's shadow region, which corresponds to the analysis where the minimum and the maximum values for the $\tau_t^{cr} - \gamma_t^{cr}$ parameters were used (see Table 4). Fig. 8 shows that the numerical model is able to capture with good accuracy the load-deflection response of the beams. However, for some beams strengthened with vertical ETS bars, even the best simulations (using the bold values in Table 4) have predicted an ultimate load higher than the load measured experimentally, this may indicate that these strengthening arrangements require some further improvements in the $\tau_t^{cr} - \gamma_t^{cr}$ diagram.

Above a deflection of about 1.4 mm, the 4S-S300-90 beam exhibited an abnormal decrease of stiffness during the experimental test,

---

[1] For interpretation of color in 'Figs. 8, 17, and 18', the reader is referred to the web version of this article.
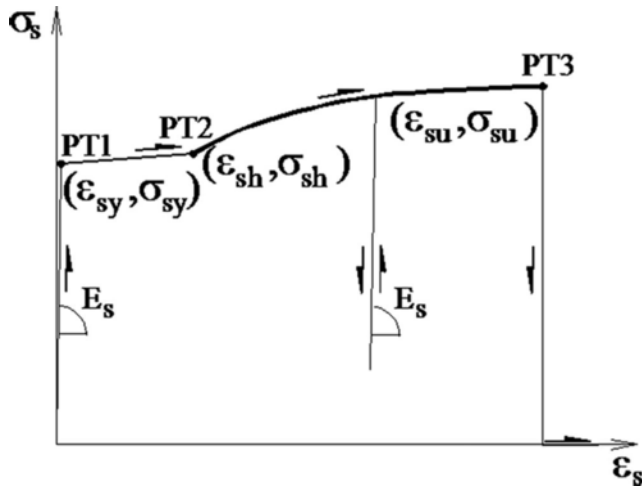
Fig. 7. Uniaxial constitutive model for the internal reinforcement and ETS bars.

when the 4S-Ref reference beam is taken for comparison purposes; therefore the model wasn't able to match the beam's behavior in this loading stage with the same accuracy.

In Fig. 9 the crack patterns obtained from the numerical simulations are superimposed with the crack patterns observed experimentally at peak load (only macro-cracks are indicated). The experimental crack patterns were captured using a close range photogrammetric technique. The localizations and inclinations of the shear failure crack and secondary cracks are captured with good accuracy. Furthermore, the shear failure mode registered experimentally in all the tested beams was successfully predicted, as can be seen by observing the localization and profile of the "fully open crack status" [12] (i.e. those unable to transfer any type of crack stress component). The model was able to simulate the relevant aspects of the crack formation and propagation during the loading process. In fact, the first cracks of a flexural nature were formed by crossing almost orthogonally the flexural reinforcement; however, due to the tension stiffening effect the width of these cracks remained relatively small. During the loading process of the beams, some of these cracks propagated towards the flange's lower surface, which averaged an inclination of 45°; meanwhile a diffuse pattern of shear cracks of very small inclination formed and propagated just above the longitudinal reinforcement due to its high dowel resistance [30]. The model was also able to register the formation of a higher number of shear cracks occurring with the increase of the reinforcing ratio of steel stirrups. In fact it is recognized that the strains measured depends significantly on the relative distance of the strain gauges (SG) from the cracks crossing the reinforcements where the SG are installed. Furthermore, when using smeared crack approaches, the cracks are distributed over the region representative of the integration point where cracks are formed, therefore as larger is the finite mesh size as smaller is the possibility of

capturing accurately the strains values recorded experimentally. Finally, assuming a perfect bond, as taken in the present simulations, a certain deviation from the strains predicted numerically and registered experimentally is being intrinsically accepted, and this deviation has tendency to increase with the loading process of the beam due to damage on the bond conditions occurred experimentally, and not simulated directly in the adopted approach. Taking these constraints, the deviations registered in Fig. 10 seem acceptable, and similar deviations have been reported by other authors when the circumstances of the analysis are identical [48]. By taking the results of the 4S-S180-45 beam, as representative, Fig. 10 evidences that the model can also predict the strain evolution in the ETS bars and steel stirrups with acceptable accuracy, since the local character of the strain measurements should be taken into account.

Based on the obtained results it seems also acceptable to assume perfect bond between strengthening material and surrounding concrete. This is especially the case if a careful evaluation of the crack width is not of paramount relevance. In fact, when steel shear reinforcements are crossed by a shear crack, due to their excellent bond conditions to the surrounding concrete, a gradient of strain in these reinforcements occurs in the cracked section, and the yield stress value is attained using a relatively small sliding and debonding length. However, the numerical simulations of RC beams shear strengthened with FRP-systems evidence the relevance of modeling the debond between FRPs and surrounding medium, due to the lower bond performance of FRP systems to the concrete substrate [56–59]. This relevance is assured by using a tau-slip constitutive model with interface finite elements, and is especially relevant when using the Externally Bonded Reinforcement (EBR) technique [23,48,60–64]. When Near-Surface Mounted (NSM) technique is used, due to the higher ratio between contact surface and cross section area of the currently used FRP laminates, as well as to the surrounding concrete's conferral of confinement on the laminates that are installed in the grooves located on the beam's concrete cover, good predictive simulations were also obtained assuming perfect bond for these FRP systems [34,65]. In the case of ETS strengthening in a similar way to the NSM FRP system the loss of bond can be ascribed in part to the concrete tensile behavior, resulting in a mixed behavior: concrete fracture and debonding [37,66,67]. In these cases, the bond-slip modeling of real scale elements is of lesser importance on global the structural behavior.

4. Parametric study

4.1. Influence of the parameters of the shear softening diagram

The numerical simulations presented in the previous section have indicated that the force-deflection and the crack pattern are susceptible to the values adopted for the parameters that define the crack shear softening diagram, namely, $\tau_{t,p}^{cr}$, β and $G_{f,s}$ (Fig. 2). In order to

Table 5
Values of the parameters of the steel constitutive model [11].

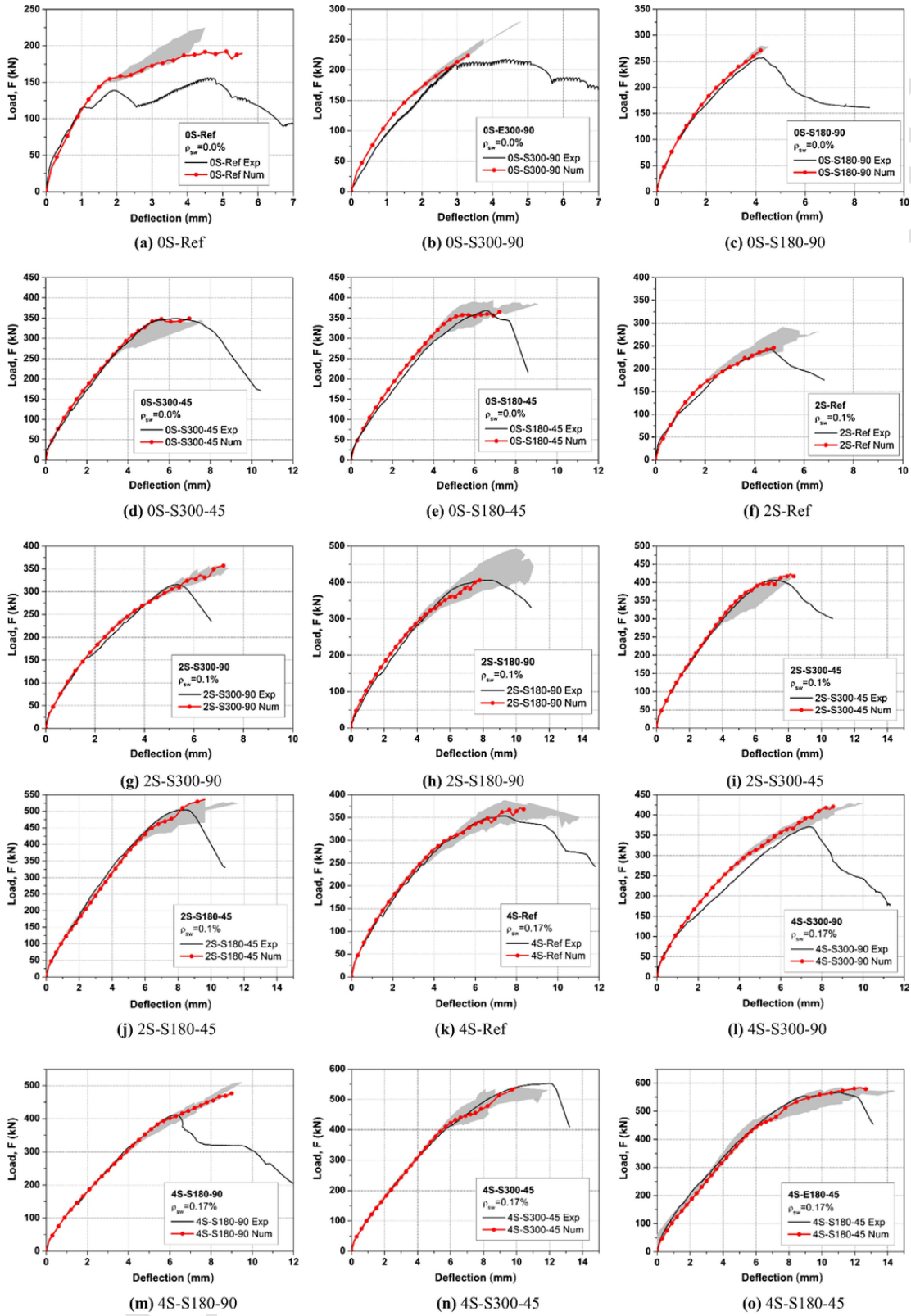| Steel bar diameter (mm)	PT1		PT2		PT3		p
	ε_{sy} [–]	σ_{sy} [MPa]	ε_{sh} [–]	σ_{sy} [MPa]	ε_{su} [–]	σ_{sy} [MPa]	
6	2.870×10^{-3}	573.94	2.870×10^{-3}	573.94	6.925×10^{-2}	666.67	1
8	2.530×10^{-3}	505.35	2.759×10^{-2}	505.35	1.280×10^{-1}	594.11	1
10	2.747×10^{-3}	549.35	2.750×10^{-2}	549.35	1.125×10^{-1}	641.83	1
12	2.637×10^{-3}	527.30	2.830×10^{-2}	527.30	1.000×10^{-2}	616.48	1
24	2.989×10^{-3}	597.88	2.989×10^{-3}	597.88	6.000×10^{-2}	708.07	1

Fig. 8. Comparison between experimental and numerical - load vs. deflection - relationship at the loaded section.
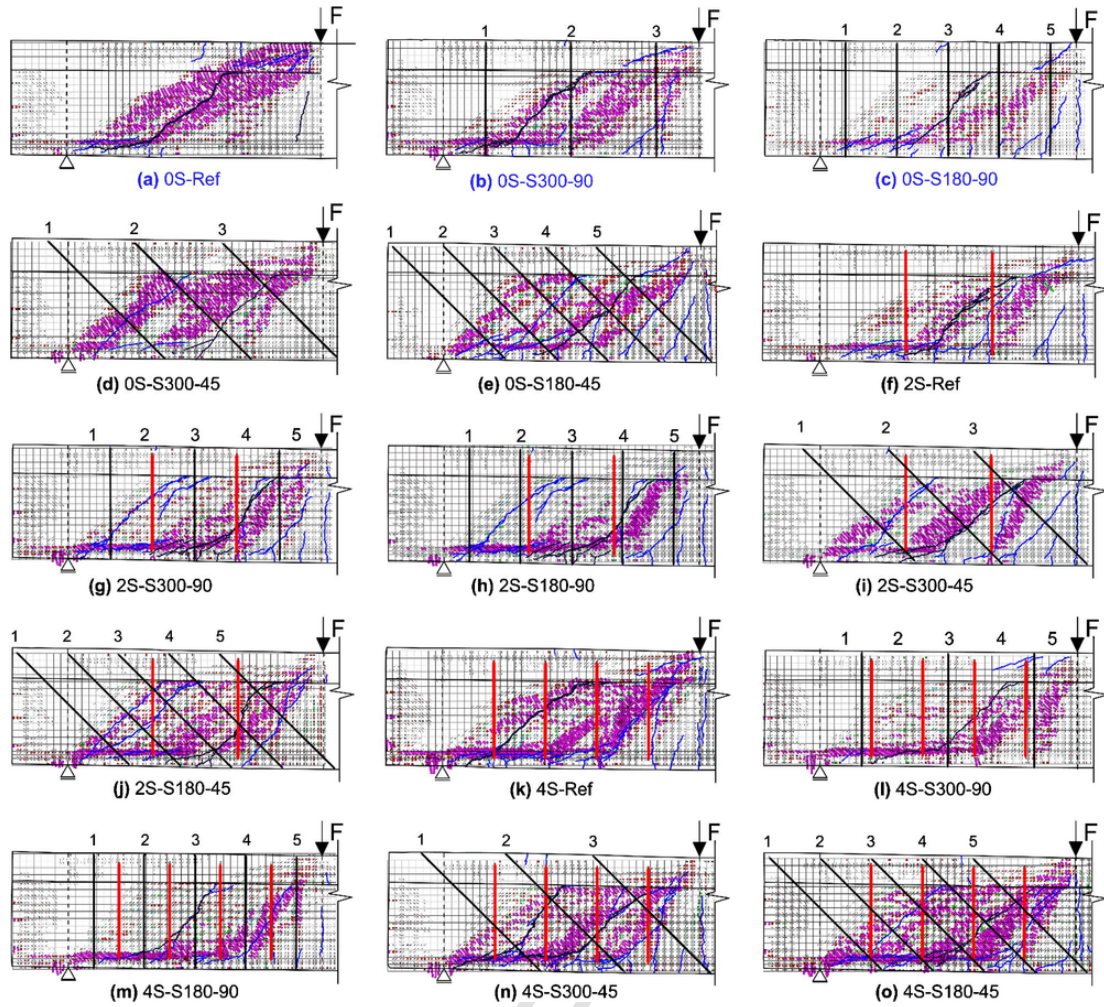
Fig. 9. Comparison between the experimental and numerical crack patterns. In the figure experimental macro-cracks are reported in dark-blue and secondary cracks in light-blue while "fully open" numerical cracks are reported in pink. (For interpretation of the references to color in this figure legend, the reader is referred to the web version of this article.)
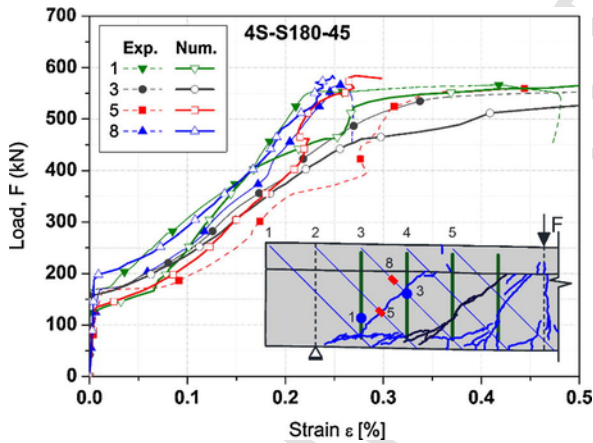

Fig. 10. Comparison between numerical and experimental strain measurement for beam 4S-S180-45.

have a better understanding of these parameters' influence on the model's predictive behavior, a parametric study was executed by considering a beam with 3 stirrups (ϕ6 mm) spaced at 225 mm: 3S-Beam. This reinforcement arrangement can be representative of real

beams deficiently reinforced in shear. The experimental load-deflection relationship of the tested beams 2S-Ref (ϕ6 mm spaced at 300 mm) and 4S-Ref (ϕ6 mm spaced at 180 mm) are compared in Figs. 11–14. The 3S-Beam simulation is depicted using a small-dashed red curve in Figs. 11–14, and is characterized by $\tau_{t,p}^{cr}$, β and $G_{f,s}$ equal to 0.15, 1.0 (MPa) and 0.08 (N/mm), respectively. As expected the 3S-Beam load deflection numerical curve lies in between the 2S-Ref and 4S-Ref experimental curves. For each selected parameter a set of values is considered, while maintaining constant all the values adopted for the remaining parameters of the multi-directional fixed smeared crack.

4.1.1. Influence of $G_{f,s}$-fracture energy mode II

Fig. 11 compares the load vs. deflection at loaded section obtained for three different values of the fracture energy mode II ($G_{f,s}$): 0.01, 0.08 and 1.5 N/mm (all the remaining parameters were maintained the same). This figure also compares the crack patterns obtained in the simulations corresponding to the assumed values of $G_{f,s}$. As expected, decreasing the $G_{f,s}$, the beam's stiffness also diminished since more cracks enter in the shear softening stage at smaller deflection. By decreasing the $G_{f,s}$, the beam's load carrying capacity undergoes a slight decrease. The use of a low value of $G_{f,s}$ gives a
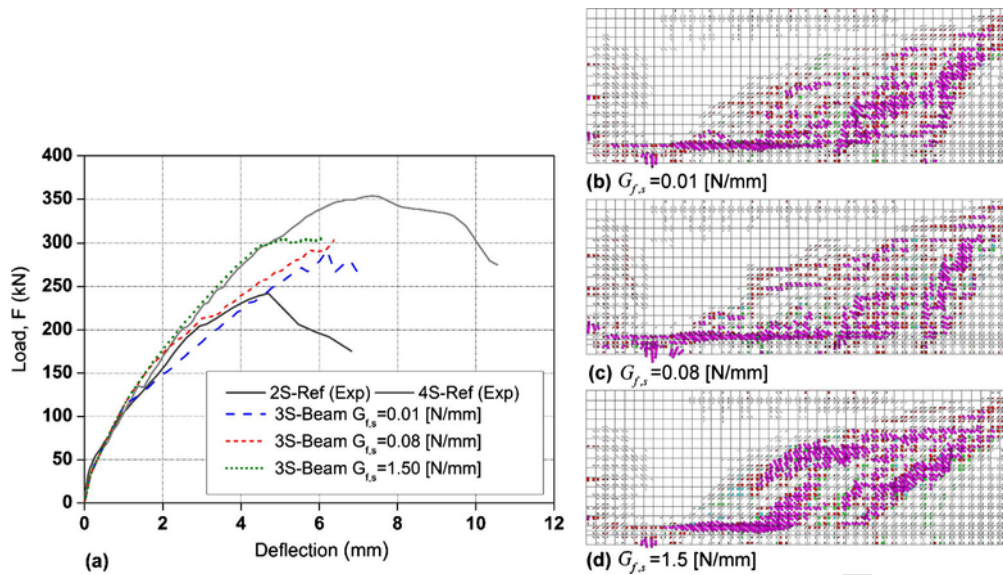
Fig. 11. Influence of $G_{f,s}$: (a) relationship between the force and the deflection at the loaded section and (b–d) crack pattern corresponding to the assumed $G_{f,s}$ at 6 mm.
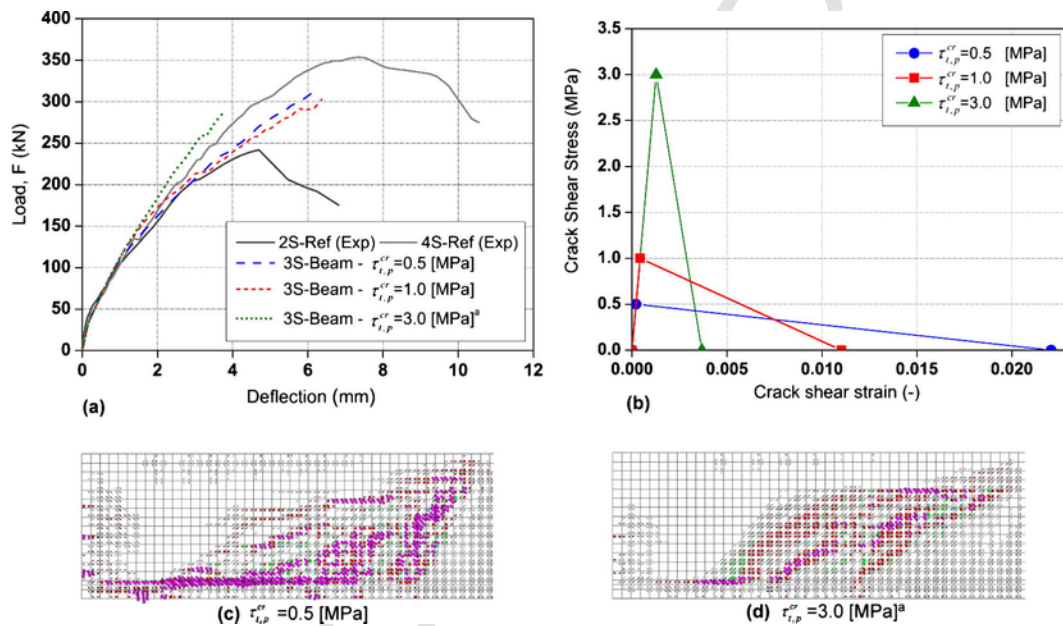

Fig. 12. Influence of $\tau_{t,p}^{cr}$: (a) relationship between the force and the deflection at the loaded section, (b) representation of the crack shear stress-shear strain diagram for the adopted $\tau_{t,p}^{cr}$, (c–d) crack pattern corresponding to the assumed $\tau_{t,p}^{cr}$. [a] The simulation was stopped due to convergence problems – crack pattern evaluated at the last point of convergence.

higher inclination of the critical shear crack which develops in proximity of the load section (as shown in Fig. 11b), as well as a tendency to form cracks localized just above the longitudinal reinforcement (Fig. 11c and d). Fig. 11d evidences that when using the highest value of $G_{f,s}$ the critical shear crack tends to have a smaller inclination.

4.1.2. Influence of crack shear strength, $\tau_{t,p}^{cr}$

Fig. 12 compares the load vs. deflection at loaded section obtained for three different values of the crack shear strength $\tau_{t,p}^{cr} = 0.5$, 1.0 and 3.0 MPa (all the remaining parameters were maintained the

same). The force-deflection response's stiffness just after the critical shear cracks' formation increases with the growth of the $\tau_{t,p}^{cr}$, since the cracks' entrance into the shear softening stage is postponed; however, after the cracks have entered into this stage, the stiffness degradation increases with the growth of $\tau_{t,p}^{cr}$ due to the more abrupt shear stress decay. In this analysis, since the $G_{f,s}$ is maintained constant, the softening response for this diagram becomes more brittle as the $\tau_{t,p}^{cr}$ rises, due to the decrease of the ultimate crack shear strain, $\gamma_{t,u}^{cr}$ (Fig. 12b). The $\tau_{t,p}^{cr}$ seems to have no major influence on the maximum load carrying capacity on this type of beams. The analysis corresponding to $\tau_{t,p}^{cr} = 0.5$ and 1.0 MPa shows approximately the same
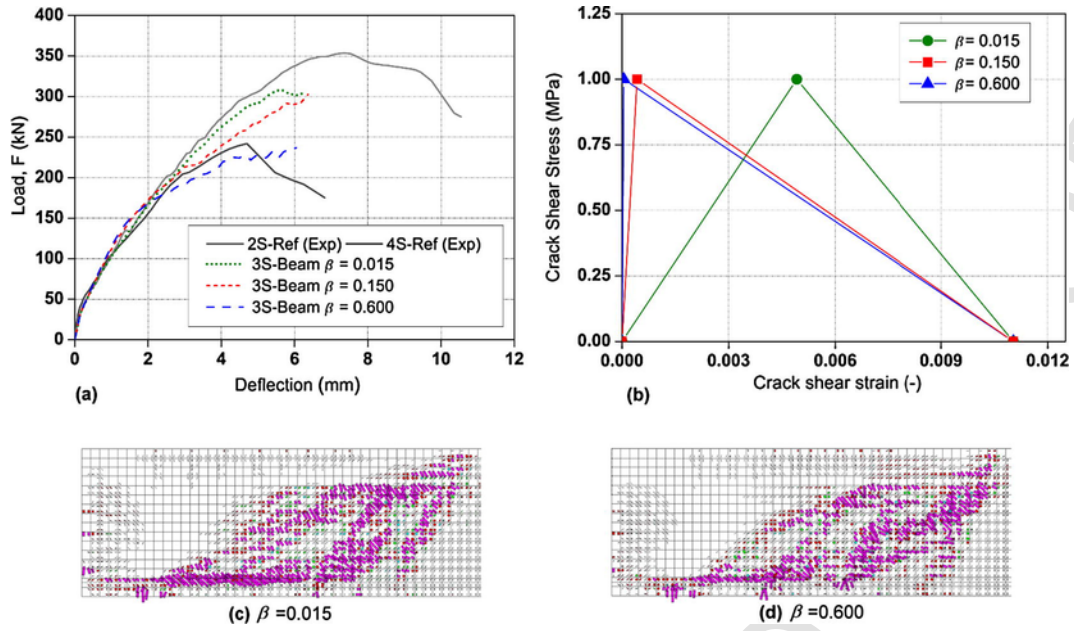
Fig. 13. Influence of β: (a) relationship between the force and the deflection at the loaded section, (b) representation of the crack shear stress-shear strain diagram for the adopted β, (c–d) crack pattern corresponding to the assumed β at 6 mm.
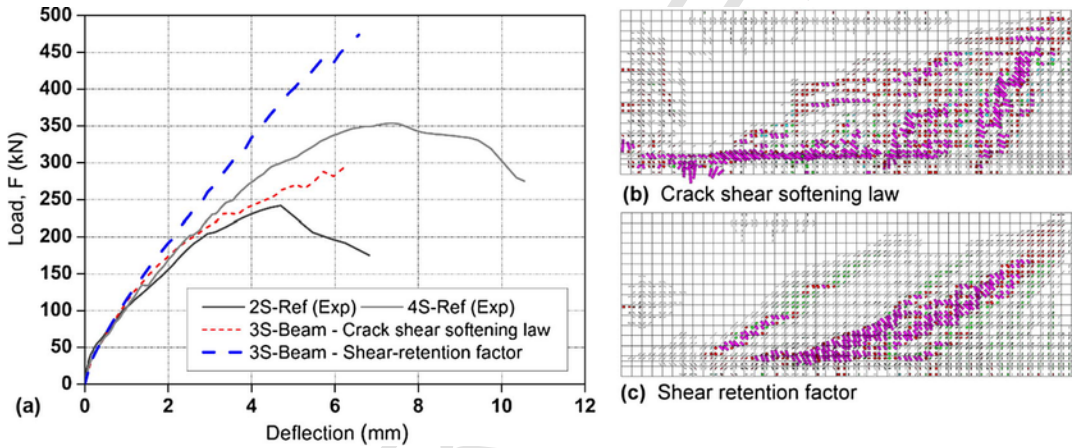

Fig. 14. (a) Comparison between the proposed crack shear softening law and the shear retention function ($p_1 = 3$); crack patterns at 6 mm obtained using the (b) crack shear softening law (c) shear retention factor.

maximum load carrying capacity, while the analysis corresponding to the $\tau_{t,p}^{cr}$ = 3 MPa was interrupted due to difficulties in the convergence procedure. For this latter simulation a significant stiffness reduction is expected as the shear cracks enter in the softening phase. From the crack patterns it is possible to observe that for the larger $\tau_{t,p}^{cr}$ (3 MPa) a smaller number of well-defined shear failure cracks (completely open) were formed when compared to the crack pattern of the smaller $\tau_{t,p}^{cr}$ (0.5 MPa), Fig. 12c and d. Furthermore, it was observed that for the $\tau_{t,p}^{cr}$ = 0.5 MPa the shear failure crack has the tendency of propagating just above the longitudinal reinforcement.

4.1.3. Influence of the β parameter

Fig. 13 compares the load vs. deflection at loaded section obtained for three different values of the shear retention parameter that influ-

ences the inclination of the first branch of the $\tau_t^{cr} - \gamma_t^{cr}$ diagram: β = 0.015, 0.15 and 0.6 (all the remaining parameters were maintained the same). The inclination of this first branch, $D_{t,1}^{cr}$, is defined by the value adopted for the β parameter according to Eq. (6), by obtaining the peak crack shear strain, $\gamma_{t,p}^{cr}$, from Eq. (9). Fig. 13b shows that the gradient of crack shear stress in this first branch decreases with β (smaller inclination of this branch). As a consequence, the stiffness of the force-deflection just after the formation of the critical shear crack also decreases with β. However, since the peak crack shear strain, $\gamma_{t,p}^{cr}$, increases as β decreases (Fig. 2), the entrance of the cracks in their softening stage is postponed, resulting in a larger stiffness of the force-deflection response for smaller β values in the final stage of the beams' response. Similar crack patterns for β = 0.015 and β = 0.6 are presented in Fig. 13c and d.

4.2. Comparison between the shear retention function and the shear softening law approach

Fig. 14 compares the relationship between the force and the deflection at loaded section for the 3S-Beam when using the shear retention function, β, (Eq. (7) with $p_1 = 3$) and adopting the $\tau_t^{cr} - \gamma_t^{cr}$ diagram. Even using relatively large values for p1 parameter, previous works [32,53] demonstrate this approach provides unsafe predictions in structures failing in shear-tension. Up to a deflection of about 1 mm (which corresponds to the formation of the shear failure crack) the responses are similar, because up to this stage, the curves are governed by concrete's tensile behavior. Above this deflection limit the two approaches start to diverge significantly. The shear-retention factor approach, implemented in an incremental model, is not able to simulate the stiffness degradation induced by the shear deformation, i.e. it is not capable of simulating a decrease of the crack shear stress transfer τ_t^{cr} with the increase of the crack shear γ_t^{cr}, and a much higher load carrying capacity than the one predicted when using the $\tau_t^{cr} - \gamma_t^{cr}$ diagram is obtained. The shear-retention factor approach has also incorrectly predicted a flexural failure mode.

5. Analytical evaluation of the β - factor and shear fracture energy $G_{f,s}$

5.1. β - factor and shear fracture energy $G_{f,s}$ as a function of the total shear reinforcement stiffness and concrete compressive strength

In order to simulate the tested beams, different values of the parameters β and $G_{f,s}$ were used. Observation highlights that these parameters play a relevant role on the beams' deformational behavior, affecting their final response. The parametric study demonstrates that the $\tau_{t,p}^{cr}$ also influences the numerical response, even though this value was assumed to be constant ($\tau_{t,p}^{cr} = 1.0$ MPa). Future works by the authors are going to be dedicated to shed light on this line of inquiry. The use of different β and $G_{f,s}$ parameters for each beam can be explained and justified by considering the fact that the adopted concrete constitutive model, which describes the behavior of plain concrete and the reinforcement modeled as embedded cable (EC), can exclude some minor concrete contribution to shear strength. It is known that effects, such as aggregate interlock and dowel action which are influenced by the percentage of transverse steel reinforcement, occur along a shear diagonal crack (Fig. 15) [68]. The presence of a high percentage of reinforcement provides additional confinement, generating an opposing force to the crack opening, which is followed by an enhancement of the aggregate interlock effect in the
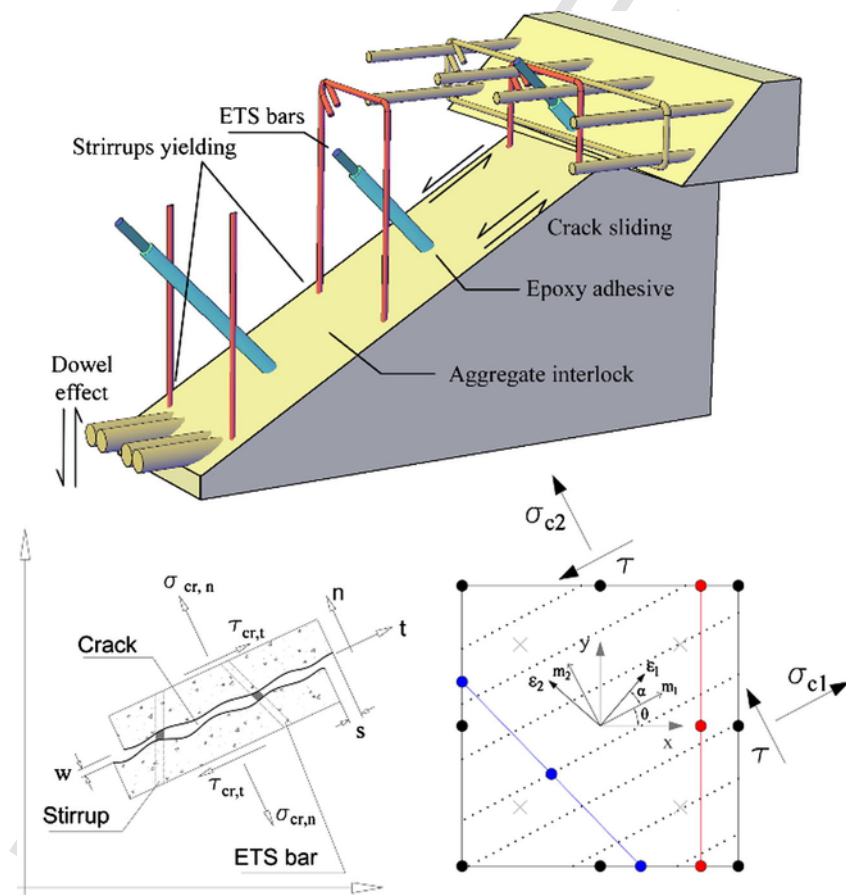

Fig. 15. Graphical representation of the shear crack plane comprehensive of the different effect and forces acting on it, bidimensional crack stress components, displacements and local coordinate system of the crack and 8-noded finite plane stress element (PSTE) with 3-noded embedded cables (EC).

shear cracks crossed by the reinforcement [69]. An et al. [18] highlighted that the shear fracture energy mode II also in plain concrete cannot be considered a material property, unlike the tensile fracture energy mode I, but it highly depends on the crack opening or confinement. This means that the steel reinforcement crossing the crack influences the crack shear stress behavior due to the external confinement it exerts. In fact, by increasing $G_{f,s}$ the beam's stiffness and load carrying capacity also increase, which indirectly simulates the favorable effect of the shear reinforcements on the aggregate interlock and dowel action. In the light of these considerations, the shear fracture energy mode II, was not assumed as material property, but it was empirically correlated to the beams mechanical and geometrical's parameters as described hereafter.

The dowel action increases as the spacing between the stirrups decreases, but the embedded cable model cannot account this effect, nor for the crack sliding resisting contribution provided by the ETS bars crossing the cracks. In the attempt of considering the possible contribution of the steel reinforcement crossing the crack, Kolmar [70] proposed a shear retention function that takes into account the percentage of steel reinforcement crossing the shear plane, more recently [19,21] also introduced in the shear-slip modeling the contribution of both aggregate interlock and dowel action.

The values of β and $G_{f,s}$ obtained by inverse analysis in Section 3.3 are plotted versus the $(E_{fw}\rho_{fw} + E_{sw}\rho_{sw}) / \left(f_{cm}^{2/3} \right)$ in Fig. 16. $(E_{fw}\rho_{fw} + E_{sw}\rho_{sw}) / \left(f_{cm}^{2/3} \right)$ depicts the total stiffness of the shear reinforcement divided by the $f_{cm}^{2/3}$ which represents the influence of the concrete compressive strength [71]. By means of a statistical linear regression analysis (LR), two equations were determined for each investigated parameter (β and $G_{f,s}$). Due to a significant experimental difference between 90° and 45° ETS installed bars, different equations were adopted for vertical (90°) and inclined (45°) strengthening. The regression lines corresponding to Eqs. (13)–(16) are reported in Fig. 13. For Eqs. (15) and (16) the constant term (Y-intercept) was set equal to $G_{f,s} = 0.07$ N/mm, the value of shear fracture energy corresponding to the beam without any shear reinforcement (0S-Ref). The inclined and vertical ETS bars are indicated with continuous and dotted lines, respectively. Fig. 16a presents the regression corresponding to the parameter, β; the diagram shows that this parameter decreases with the increase of $(E_{fw}\rho_{fw} + E_{sw}\rho_{sw}) / \left(f_{cm}^{2/3} \right)$. Simi-

lar inclinations were obtained for vertical and inclined ETS bars; nevertheless, higher values of β were provided for vertical (90°) ETS bars. Fig. 16b presents the regression corresponding to the parameter, $G_{f,s}$, and shows that it increases with the increment of $(E_{fw}\rho_{fw} + E_{sw}\rho_{sw}) / \left(f_{cm}^{2/3} \right)$, which as previously explained, can be justified by the favorable effect provided by the steel reinforcement on the aggregate interlock, dowel action and crack sliding. Higher values of $G_{f,s}$ and higher slope of the linear regression were obtained for inclined (45°) ETS bars. The coefficient of determination R^2 shows a dispersion of data in the range of 0.46 and 0.94.

$$\beta = -1.14 \cdot [(E_{fw}\rho_{fw} + E_{sw}\rho_{sw})/(f_{cm}^{2/3})] + 0.176 \quad R^2 = 0.46 \quad \text{LR for}$$

$$\beta = -1.36 \cdot \left[(E_{fw}\rho_{fw} + E_{sw}\rho_{sw}) \Big/ \left(f_{cm}^{2/3} \right) \right] + 0.$$

$$G_{f,s} = 2.15 \cdot \left[(E_{fw}\rho_{fw} + E_{sw}\rho_{sw}) \Big/ \left(f_{cm}^{2/3} \right) \right] + 0$$

$$G_{f,s} = 9.77 \cdot \left[(E_{fw}\rho_{fw} + E_{sw}\rho_{sw}) \Big/ \left(f_{cm}^{2/3} \right) \right] + 0$$

5.2. Assessment of the predictive performance

With the aim to assess the predictive performance of the proposed equations for estimating the value of the parameters β and $G_{f,s}$, the numerical response of two groups of beams was evaluated using the values calculated by Eqs. (13)–(16). The first group is represented by the tested beams used to calibrate the constitutive model whereas the second group is represented by the ETS shear strengthened beams tested by Barros and Dalfré [29]. In the authors' opinion, as a result
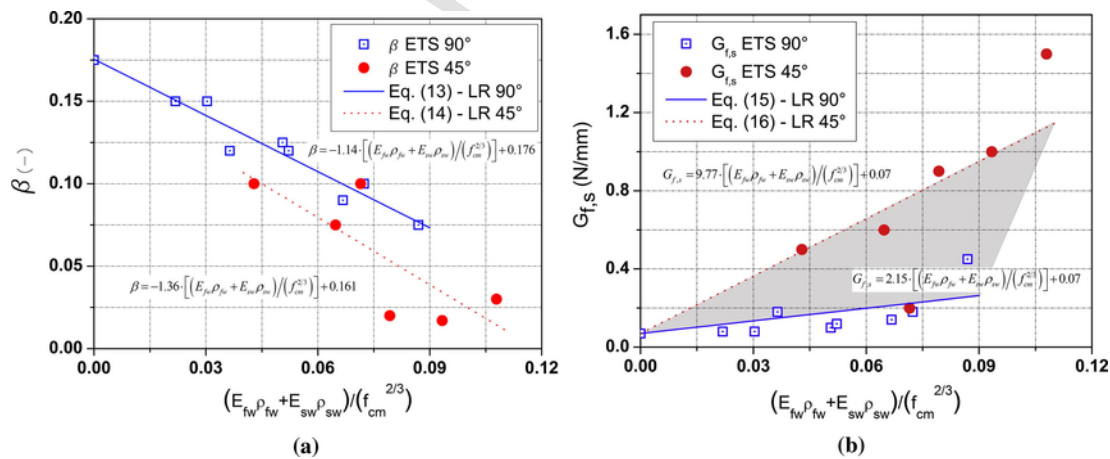

Fig. 16. β - factor (a) and shear fracture energy $G_{f,s}$ (b) as a function of the total shear reinforcement stiffness and concrete compressive strength. LR stands for linear regression.

of the high dispersion of data observed in the linear regressions (LR), it is reasonable to simulate the same beams used to fit the parameters β and $G_{f,s}$, in order to evaluate how the relative high dispersion could affect the results; moreover the parameters have been calibrated independently of each other.

For the first group of beams Table 6 reports the values calculated by Eqs. (13)–(16); they are compared to the values derived from pa-

Table 6
Comparison between the calibrated values and values calculated by Eqs. (13)–(16).

	β [–]	β [–] Eqs. (13) and (14)	$G_{f,s}$ [N/mm]	$G_{f,s}$ [N/mm] Eqs. (15) and (16)
0S-Ref	0.175	0.176	0.07	0.070
0S-S300-90	0.15	0.141	0.08	0.135
0S-S180-90	0.144	0.118	0.1	0.178
0S-S300-45	0.175	0.103	0.50	0.489
0S-S180-45	0.1	0.064	0.20	0.768
2-Ref	0.15	0.151	0.08	0.117
2S-S300-90	0.12	0.116	0.12	0.182
2S-S180-90	0.1	0.093	0.18	0.225
2S-S300-45	0.075	0.073	0.6	0.702
2S-S180-45	0.017	0.034	1.00	0.981
4S-Ref	0.1	0.134	0.22	0.148
4S-S300-90	0.09	0.100	0.14	0.213
4S-S180-90	0.075	0.077	0.45	0.256
4S-S300-45	0.02	0.053	0.9	0.844
4S-S180-45	0.030	0.014	1.5	1.124

rameters' calibration and presented in Section 3.3. The obtained load-deflection relationship and crack patterns of selected beams are presented in Figs. 17 and 18, respectively; further results can be found in [72]. The red color curves, including circle full markers, were obtained by using the calibrated values (bold character in Table 4), while the blue color curves, including square empty markers, were obtained by using the parameter values calculated by Eqs. (13)–(16). It is possible to notice that, in most of the cases, these latter curves are very similar to the load-deflection responses obtained experimentally. Some of these simulations overestimate (for example beam 0S-S180-45 or 2S-S180-90) or underestimate (for example beam 2S-S300-45) the beams' load carrying capacity, mainly when an appreciable difference between the values β and $G_{f,s}$ in Table 6 is found. Nevertheless, as can be seen in general, even in the presence of significant difference, satisfactory results are obtained. In some of the numerical simulations an underestimation of the maximum load carrying capacity can be attributed to numerical instabilities (e.g. 4S-S180-45). The crack patterns reported in Fig. 18 indicate a good agreement between numerical and experimental results. This first group of simulations highlights the potentiality to increase the values of $G_{f,s}$ and decrease the value of β with the increment of the total stiffness of the shear reinforcement $(E_{fw}\rho_{fw} + E_{sw}\rho_{sw})$.

The second group of beams [29] consisted of rectangular beams of different rectangular cross sections and a constant L_1/d ratio of 3.44. A-Series (150×300 mm^2) and B-Series (300×300 mm^2) are characterized by a ρ_{sl} of 2.5 and 1.88% respectively. The internal percentage of transverse internal steel reinforcement varied in the range of 0.0% and 0.17%, and the percentage of strengthening ETS bars, vertical or inclined (45°), varied in the range of 0.6% and 25%. The concrete compressive strength ranged between 28.8 MPa and 30.8 MPa. More details about this experimental program can be found in Barros and Dalfrè [29]. The adopted modeling strategy is equal to the one described in Section 3.2. The main values that define the concrete constitutive model are indicated in Table 7; they were obtained, to-
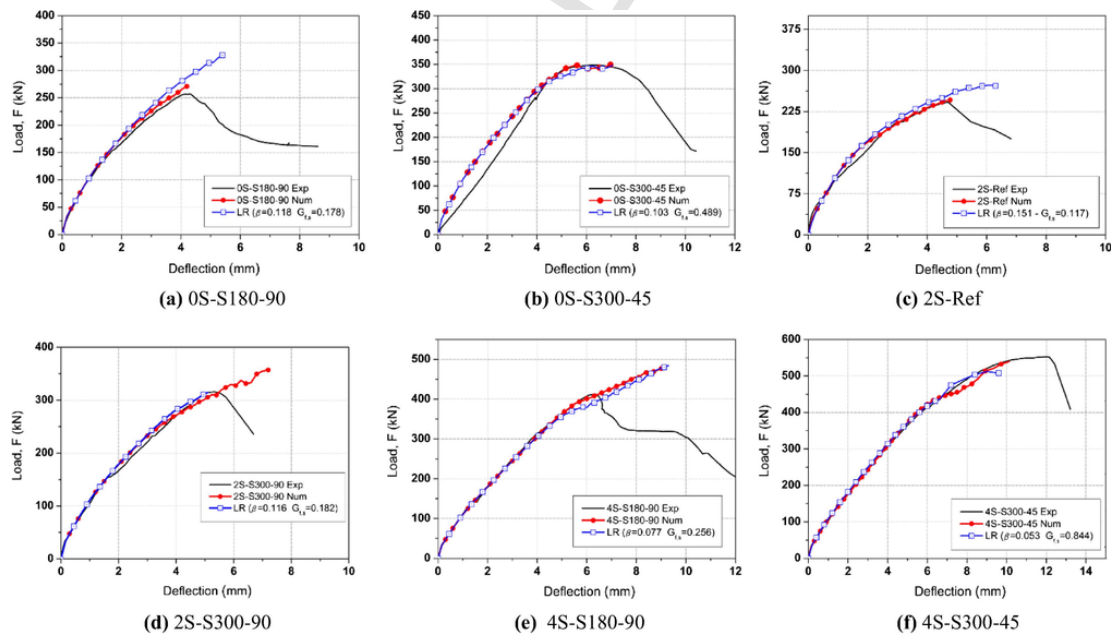
Fig. 17. Numerical load versus deflection at loaded section using the β, $G_{f,s}$ values calculated by Eqs. (13)–(16) (blue color curves, including square empty markers – linear regression (LR); comparison with experimentally calibrated values (red color, including circle markers). (For interpretation of the references to color in this figure legend, the reader is referred to the web version of this article.)
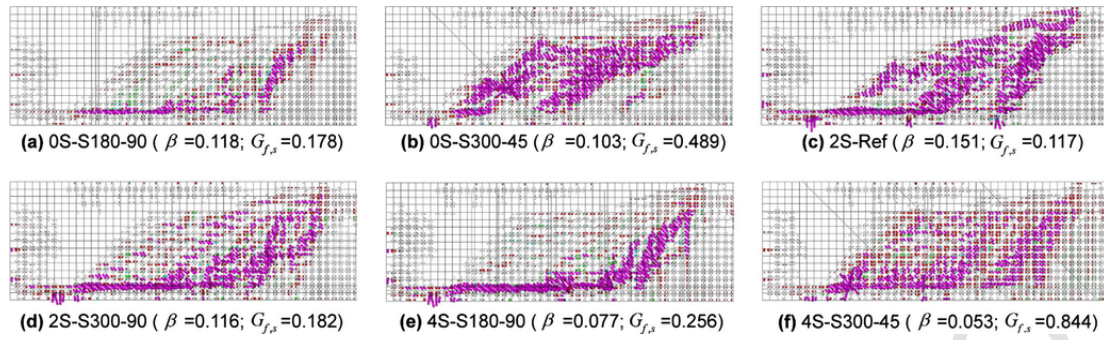
Fig. 18. Crack-patterns obtained using the β and $G_{f,s}$ values calculated by Eqs. (13)–(16).

Table 7
Main values of the parameters of the concrete constitutive model used to simulate the beams tested by Dalfré and Barros [17].

Poisson's ratio (ν_c)	0.15
Initial Young's modulus (E_c)	31.1 N/mm^2
Compressive strength (f_c)	30.7 N/mm^2
Trilinear tension-softening diagram	$f_{ct} = 1.9$ N/mm^2, $G_f = 0.08$ N/mm
	$\xi_1 = 0.01$, $\alpha_1 = 0.5$, $\xi_2 = 0.7$, $\alpha_2 = 0.2$

Note: if not specified the model's parameters are equal to the ones specified in Table 3.

gether with the values defining the steel and ETS bars constitutive model, from a previous set of numerical simulation (only small changes to the trilinear stress-strain diagram were made) [33]. The simulations of eight beams which exhibited a clear shear failure are represented here. Table 8 indicates the designation adopted for the beams in Barros and Dalfré [29], percentage of steel stirrups (ρ_{sw}), the shear strengthening ratio ρ_{fw}, as well as the values of β and $G_{f,s}$ calculated by Eqs. (13)–(16) for the crack shear softening diagram. The $\tau_{t,p}^{cr}$ was assumed equal to 1.38 MPa, which corresponds to 0.14"–"0.15$f_{cm}^{2/3}$, this value was previously adopted in [33]. The obtained load-deflection relationship are presented in Fig. 19. The blue color curves, including square empty markers are obtained by using the values calculated by Eqs. (13)–(16); the figure also shows the experimental crack pattern and the position of stirrups and ETS bars. In

Table 8
Percentage of internal stirrups (ρ_{sw}), ETS strengthening (ρ_{fw}) and β and $G_{f,s}$ values calculated by Eqs. (13)–(16) for the beams tested by Dalfré and Barros [17].

	ρ_{sw} [%]	ρ_{fw} [%]	β [–] Eqs. (13) and (14)	$G_{f,s}$ [N/mm] Eqs. (15) and (16)
A.1-Reference[a]	–	–	0.176	0.070
A.2-S300.90[a]	0.13	–	0.145	0.129
A.3-E300.90[a]	–	0.17	0.136	0.146
A.4-E300.45[b]	–	0.25	0.087	0.603
B.1-Reference[a]	–	–	0.176	0.070
B.2-S300.90[a]	0.06	–	0.162	0.097
B.3-E300.90[a]	–	0.11	0.149	0.121
B.4-E300.45[b]	–	0.16	0.112	0.423

[a] Compressive strength f_{cm} = 30.78 MPa.

[b] Compressive strength f_{cm} = 28.81 MPa.

terms of the load-deflection response, good predictive performance is shown in Fig. 19 where the maximum load carrying capacity is estimated with sufficient accuracy. A comparison of this group of beams' deflectional behavior and the predicted load carrying capacity shows that the values obtained from the linear regression provide more than reasonable results when utilized to characterize the shear softening law.

In general the results affirm that the presented equations (Eqs. (13)–(16)) can be considered a suitable tool to obtain a first estimation of the parameters β and $G_{f,s}$; however for similar geometry of ETS strengthened RC beams, higher number of test should be performed to confirm a general validity. Since all the simulated beams are characterized by similar concrete compressive strength, it is impossible to evaluate the impact of the term $f_{cm}^{2/3}$ on the provided equations, further investigations on the influence of the concrete compressive are needed.

6. Conclusion

The analysis capability of a multi-directional fixed smeared crack model FE program (FEMIX) to estimate the behavior of RC beams shear strengthened using steel ETS bars was assessed. In order to simulate the stiffness degradation of the shear modulus after crack initiation, a shear softening law $\left(\tau_t^{cr} - \gamma_t^{cr} - \text{diagram}\right)$ was adopted as alternative to the shear retention function. The parameters, β, $\tau_{t,p}^{cr}$, $G_{f,s}$ characterizing the crack shear stress – crack shear strain diagram were identified by calibrating the experimental results, since to the authors' knowledge, there are no experimental tests dedicated to the assessment of these parameters. For each tested beam a different shear softening diagram was identified, nevertheless $\tau_{t,p}^{cr}$ was assumed equal to 1.0 MPa for all the beams, in the attempt to reduce the number of variables.

The performed numerical simulations have reproduced with high accuracy the deformational behavior of the experimental tests, as well as the crack pattern and strains in stirrups and ETS bars. In general, a fairly good prediction of the load carrying capacity was found. It was also demonstrated that, due to the good bond performance between ETS bars and concrete during the experimental tests, the assumption of perfect bond between materials is acceptable and valid results can be obtained. The numerical simulation evidenced that $G_{f,s}$ exhibits the tendency to increase with the percentage of transverse reinforcement, which can be justified by the positive impact on aggregate interlock provided by the steel bars crossing the cracks; this is the opposite of the β - factor, which exhibits the tendency to decrease with the percentage of transverse reinforcement. The performed parametric study highlighted that the values defining the shear softening law
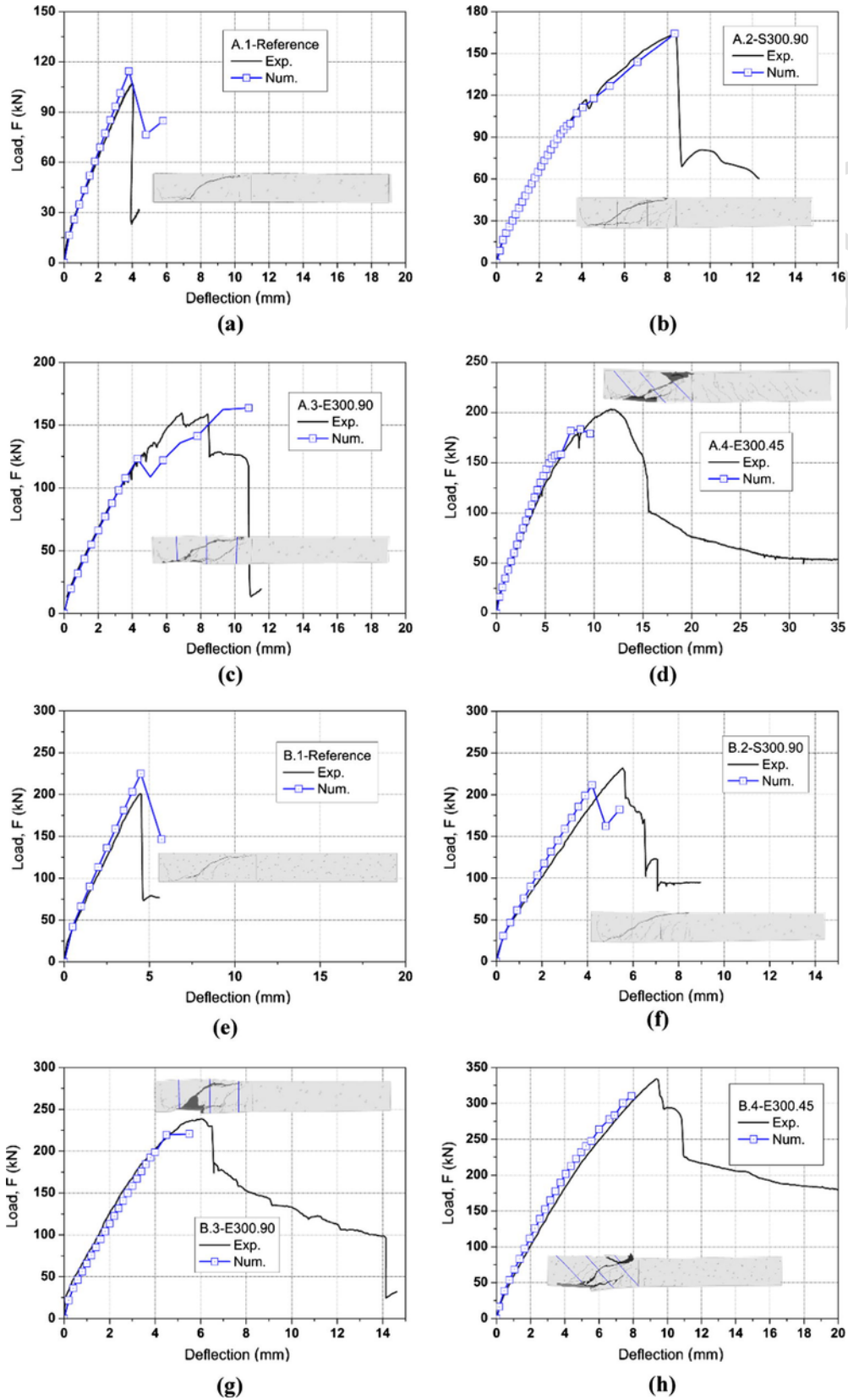
Fig. 19. Experimental [17] and numerical load versus the deflection at loaded section. β, $G_{f,s}$ values calculated by Eqs. (13)–(16).

mainly influenced the deformational response and the crack pattern at failure; in general, less influence was observed in the prediction of the maximum load carrying capacity.

It is possible to conclude that one of the key aspects of the $\tau_t^{cr} - \gamma_t^{cr}$ diagram is the characterization of its softening branch; the numerical simulations evidenced the importance of the point where the element enters in the softening phase, as well as its ultimate crack shear strain. It was shown that, by using the linear regression model to estimate the values of β, $G_{f,s}$ based on the numerical simulation of the tested beams, it is possible to estimate the structural response in terms of load-deflection with satisfactory results. The present work has shown the potential of evaluating with sufficient accuracy the β, $G_{f,s}$ as a function of the total transverse reinforcement stiffness and the concrete compressive strength. Nevertheless, more investigation is needed to provide a general rule for the estimation of the $\tau_t^{cr} - \gamma_t^{cr}$ diagram for RC un-strengthened and strengthened elements.

It was observed that, by adopting a shear retention function, the level of stiffness degradation registered in the tested beam was not correctly simulated, and a much higher ultimate load was estimated. Very good predictions are, however, capable of being assured if a proper $\tau_t^{cr} - \gamma_t^{cr}$ is adopted. It can be concluded that - by adopting the shear softening law in the multidirectional fixed smeared crack model, available in the FEMIX computer program - the numerical analysis was able, with higher accuracy, to predict the behavior of structures failing in shear while the numerical capability also improved.

Acknowledgements

References

[1] J.G. Rots, P. Nauta, G.M.A. Kusters, J. Blaauwendraad, Smeared crack approach and fracture localization in concrete, HERON 30 (1) (1985) 1–48.

[2] R. de Borst, P. Nauta, Non-orthogonal cracks in a smeared finite element model, Eng Comput 2 (1) (1985) 35–46, http://dx.doi.org/10.1108/eb023599.

[3] K. Maekawa, A. Pimanmas, H. Okamura, Nonlinear mechanics of reinforced concrete, CRC Press, 2003768.

[4] Rots JG. Comparative study of crack models. In: Hendriks MAN, Rots JG, AA, editor. Third DIANA world conf, Tokyo, Japan 9–11 October. Taylor & Francis; 2002, p. 17–28.

[5] H.-G. Kwak, F.C. Filippou, Finite element analysis of reinforced concrete structures under monotonic loads, REPORT NO. UCB/SEMM-90/14 University of California Berkeley, 1990.

[6] H.-T. Hu, W.C. Schnobrich, Nonlinear analysis of cracked reinforced concrete, ACI Struct J 87 (2) (1990) 199–207, http://dx.doi.org/10.14359/2706.

[7] ASCE. State-of-the-art report on finite element analysis of reinforced concrete; 1982.

[8] L. Cedolin, Poli S. Dei, Finite element studies of shear-critical R/C beams, J Eng Mech Div 103 (3) (1977) 395–410.

[9] W. Kolmar, G. Mehlhorn, Comparison of shear stiffness formulations for cracked reinforced concrete elements, In: Proc: int conf on comput aided anal des concr struct, Part1, split, Yugoslavia, 1984, pp. 133–147.

[10] J.G. Rots, Computational modeling of concrete fracture, PhD Thesis Delft University of Technology, The Netherlands, 1988.

[11] J.A.O. Barros, Comportamento do betão reforçado com fibras. Análise experimental e simulação numérica. Behavior of fiber reinforced concrete. Experimental analysis and numerical simulation, Ph.D. Thesis Department of Civil Engineering, University of Porto, 1995.

[12] J.M. Sena-Cruz, Strengthening of concrete structures with near-surface mounted CFRP laminate strip, Ph.D. Thesis Department of Civil Engineering, University of Minho, 2004.

[13] Z.P. Bazant, P. Gambarova, Rough cracks in reinforced concrete, J Struct Div ASCE 106 (1980) 297–315.

[14] J.C. Walraven, H.W. Reinhardt, Theory and experiments on the mechanical behaviour of cracks in plain and reinforced concrete subjected to shear loading, HERON 26 (1A) (1981) 68.

[15] B. Li, K. Maekawa, H. Okamura, Contact density model for stress transfer across cracks in concrete, J Fac Eng – Univ Tokyo 49 (1989) 9–52.

[16] H. Okamura, K. Maekawa, Non linear analysis and constitutive models of reinforced concrete, Gihodo-Shuppan, Tokyo, 1991.

[17] B. Bujadham, K. Maekawa, The universal model for stress transfer across cracks in concrete, Proc JSCE 451 (17) (1992) 277–287.

[18] X. An, K. Maekawa, H. Okamura, Numerical simulation of size effect in shear strength of RC beams, J Mater Concr Struct Pavements, JSCE 564 (35) (1997) 297–316.

[19] H. Dabbagh, S.J. Foster, A smeared – fixed crack model for FE analysis of RC membranes incorporating aggregate interlock, Adv Struct Eng 9 (1) (2006) 91–102, http://dx.doi.org/10.1260/136943306776232927.

[20] F. Vecchio, Disturbed stress field model for reinforced concrete: formulation, J Struct Eng 126 (9) (2000) 1070–1077, http://dx.doi.org/10.1061/(ASCE)0733-9445(2000)126:9(1070).

[21] R. Cerioni, I. Iori, E. Michelini, P. Bernardi, Multi-directional modeling of crack pattern in 2D R/C members, Eng Fract Mech 75 (3–4) (2008) 615–628, http://dx.doi.org/10.1016/j.engfracmech.2007.04.012.

[22] M. Pimentel, E. Brüwhiler, J. Figueiras, Extended cracked membrane model for the analysis of RC panels, Eng Struct 32 (8) (2010) 1964–1975, http://dx.doi.org/10.1016/j.engstruct.2010.02.030.

[23] J.G. Teng, S.S. Zhang, J.G. Dai, J.F. Chen, Three-dimensional meso-scale finite element modeling of bonded joints between a near-surface mounted FRP strip and concrete, Comput Struct 117 (2013) 105–117, http://dx.doi.org/10.1016/j.compstruc.2012.12.002.

[24] A. Jahanmohammadi, M. Soltani, Toward combined local-average stress field modeling of reinforced concrete, Eng Struct 111 (2016) 394–410, http://dx.doi.org/10.1016/j.engstruct.2015.11.035.

[25] J.G. Rots, R. de Borst, Analysis of mixed-mode fracture in concrete, J Eng Mech ASCE 113 (11) (1987) 1739–1758, http://dx.doi.org/10.1061/(ASCE)0733-9399(1987) 113:11(1739).

[26] A. Ventura-Gouveia, Constitutive models for the material nonlinear analysis of concrete structures including time-dependent effects, Ph.D. Thesis Department of Civil Engineering, University of Minho, 2011.

[27] P. Valerio, T.J. Ibell, A.P. Darby, Deep embedment of FRP for concrete shear strengthening, Proc ICE – Struct Build 162 (5) (2009) 311–321, http://dx.doi.org/10.1680/stbu.2009.162.5.311.

[28] O. Chaallal, A. Mofidi, B. Benmokrane, K. Neale, Embedded through-section FRP rod method for shear strengthening of RC beams: performance and comparison with existing techniques, J Compos Constr 15 (3) (2011) 732–742, http://dx.doi.org/10.1061/(ASCE)CC.1943-5614.0000174.

[29] J.A.O. Barros, G.M. Dalfré, Assessment of the effectiveness of the embedded through-section technique for the shear strengthening of reinforced concrete beams, Strain 49 (1) (2012) 75–93, http://dx.doi.org/10.1111/str.12016.

[30] M. Breveglieri, A. Aprile, J.A.O. Barros, Shear strengthening of reinforced concrete beams strengthened using embedded through section steel bars, Eng Struct 81 (2014) 76–87, http://dx.doi.org/10.1016/j.engstruct.2014.09.026.

[31] M. Breveglieri, A. Aprile, J.A.O. Barros, Embedded through-section shear strengthening technique using steel and CFRP bars in RC beams of different percentage of existing stirrups, Compos Struct 125 (2015) 101–113, http://dx.doi.org/10.1016/j.compstruct.2015.02.025.

[32] J.A.O. Barros, I.G. Costa, A. Ventura-Gouveia, CFRP flexural and shear strengthening technique for RC beams: experimental and numerical research, Adv Struct Eng 14 (3) (2011) 551–571, http://dx.doi.org/10.1260/1369-4332.14.3.551.

[33] J.A.O. Barros, M. Breveglieri, A. Ventura-Gouveia, G.M. Dalfré, A. Aprile, Model to simulate the behavior of RC beams shear strengthened with ETS bars, in: J.G.M. Mier, G. Ruiz, C. Andrade, R.C. Yu, X. Zhang (Eds.), Fram fract mech concr concr struct, CIMNE International Center for Numerical Methods in Engineering, Toledo (Spain), 2013, pp. 505–516.

[34] J.A.O. Barros, H. Baghi, S.J.E. Dias, A. Ventura-Gouveia, A FEM-based model to predict the behaviour of RC beams shear strengthened according to the NSM technique, Eng Struct 56 (2013) 1192–1206, http://dx.doi.org/10.1016/j.engstruct.2013.06.034.

[35] J.M. Sena-Cruz, J.A.O. Barros, A.F.M. Azevedo, A. Ventura-Gouveia, Numerical simulation of the nonlinear behavior of RC beams strengthened with NSM CFRP strips, In: Proc C congr, FEUP, Porto, Portugal, 13 15 June, 2007, 2007.

[36] Z.P. Bazant, B.H. Oh, Crack band theory for fracture of concrete, vol. 16(93), RILEM Publ SARL, 1983155–177.

[37] M. Breveglieri, A. Aprile, J.A.O. Barros, RC beams strengthened in shear using the embedded through-section technique: experimental results and analytical formulation, Compos Part B Eng 89 (2016) 266–281, http://dx.doi.org/10.1016/j.compositesb.2015.11.023.

[38] T. Triantafillou, Shear strengthening of reinforced concrete beams using epoxy-bonded FRP composites, ACI Struct J 95 (2) (1998) 107–115, http://dx.doi.org/10.14359/531.

[39] B. Täljsten, Strengthening concrete beams for shear with CFRP sheets, Constr Build Mater 17 (1) (2003) 15–26, http://dx.doi.org/10.1016/S0950-0618(02)00088-0.

[40] J.F. Chen, J.G. Teng, Shear capacity of FRP-strengthened RC beams: FRP debonding, Constr Build Mater 17 (1) (2003) 27–41, http://dx.doi.org/10.1016/S0950-0618(02)00091-0.

[41] A. Carolin, B. Täljsten, Theoretical study of strengthening for increased shear bearing capacity, J Compos Constr 9 (6) (2005) 497–506, http://dx.doi.org/10.1061/(ASCE)1090-0268(2005) 9:6(497).

[42] A. Bousselham, O. Chaallal, Effect of transverse steel and shear span on the performance of RC beams strengthened in shear with CFRP, Compos Part B Eng 37 (1) (2006) 37–46, http://dx.doi.org/10.1016/j.compositesb.2005.05.012.

[43] M. Pellegrino, C. Modena, Fiber-reinforced polymer shear strengthening of reinforced concrete beams: experimental study and analytical modeling, ACI Struct J 103 (5) (2006) 720–728.

[44] E. Grande, M. Imbimbo, A. Rasuolo, Effect of transverse steel on the response of RC beams strengthened in shear by FRP: experimental study, J Compos Constr 13 (9) (2009) 405–414, http://dx.doi.org/10.1061/(ASCE)1090-0268(2009) 13:5(405).

[45] S.J.E. Dias, J.A.O. Barros, Shear strengthening of RC T-section beams with low strength concrete using NSM CFRP laminates, Cem Concr Compos 33 (2) (2011) 334–345, http://dx.doi.org/10.1016/j.cemconcomp.2010.10.002.

[46] J.S. Cruz, J. Barros, Modeling of bond between near-surface mounted CFRP laminate strips and concrete, Comput Struct 82 (2004) 1513–1521, http://dx.doi.org/10.1016/j.compstruc.2004.03.047.

[47] Ventura-Gouveia A, Barros JAO, Azevedo AFM, Sena-Cruz JM. Implementação da técnica do arc-length e métodos relacionados no programa de elementos finitos FEMIX. Report 06-DEC/E-20-Universidade do Minho; 2006.

[48] G.M. Chen, J.F. Chen, J.G. Teng, On the finite element modelling of RC beams shear-strengthened with FRP, Constr Build Mater 32 (2012) 13–26, http://dx.doi.org/10.1016/j.conbuildmat.2010.11.101.

[49] A.T. Slobbe, M.A.N. Hendriks, J.G. Rots, Sequentially linear analysis of shear critical reinforced concrete beams without shear reinforcement, Finite Elem Anal Des 50 (2012) 108–124, http://dx.doi.org/10.1016/j.finel.2011.09.002.

[50] CEB-FIP Model Code 90. Bulletin d'Information N 213/214.Th. Telford, London; 1993. ISBN 0-7277-1696-4. 460 pages.

[51] A. Edalat Behbahani, J.A.O. Barros, A. Ventura-Gouveia, Plastic-damage smeared crack model to simulate the behaviour of structures made by cement based materials, Int J Solids Struct 73–74 (2015) 20–40, http://dx.doi.org/10.1016/j.ijsolstr.2015.07.027.

[52] F. Soltanzadeh, A.E. Behbahani, H. Mazaheripour, J.A.O. Barros, Shear resistance of SFRSCC short-span beams without transversal reinforcements, Compos Struct 139 (2016) 42–62, http://dx.doi.org/10.1016/j.compstruct.2015.11.06.

[53] H. Baghi, J.A.O. Barros, Shear properties of the strain hardening cementitious composite material, J Mater Civ Eng (2016) http://dx.doi.org/10.1061/(ASCE)MT.1943-5533.0001603.

[54] A. Edalat Behbahani, J.A.O. Barros, A. Ventura-Gouveia, Application of plastic-damage multidirectional fixed smeared crack model in the analysis of RC structures, Eng Struct (2016). [in press].

[55] L. Jendele, J. Cervenka, Finite element modelling of reinforcement with bond, Comput Struct 84 (28) (2006) 1780–1791, http://dx.doi.org/10.1016/j.compstruc.2006.04.010.

[56] H. Yuan, J.G. Teng, R. Seracino, Z.S. Wu, J. Yao, Full-range behavior of FRP-to-concrete bonded joints, Eng Struct 26 (5) (2004) 553–565, http://dx.doi.org/10.1016/j.engstruct.2003.11.006.

[57] V. Bianco, J.A.O. Barros, G. Monti, Bond model of NSM-FRP strips in the context of the shear strengthening of RC beams, J Compos Constr 135 (6) (2009) 619–631, http://dx.doi.org/10.1061/(ASCE)0733-9445(2009) 135:6(619).

[58] R. Seracino, N.M. Jones, M.S. Ali, M.W. Page, D.J. Oehlers, Bond strength of near-surface mounted FRP strip-to-concrete joints, J Compos Constr 11 (4) (2007) 401–409.

[59] M.S. Mohamed Ali, D.J. Oehlers, M.C. Griffith, R. Seracino, Interfacial stress transfer of near surface-mounted FRP-to-concrete joints, Eng Struct 30 (7) (2008) 1861–1868, http://dx.doi.org/10.1016/j.engstruct.2007.12.006.

[60] A.M. Sayed, X. Wang, Z. Wu, Finite element modeling of the shear capacity of RC beams strengthened with FRP sheets by considering different failure modes, Constr Build Mater 59 (2014) 169–179, http://dx.doi.org/10.1016/j.conbuildmat.2014.02.044.

[61] S.S. Zhang, J.G. Teng, Finite element analysis of end cover separation in RC beams strengthened in flexure with FRP, Eng Struct 75 (2014) 550–560, http://dx.doi.org/10.1016/j.engstruct.2014.06.031.

[62] G.C. Manos, M. Theofanous, K. Katakalos, Numerical simulation of the shear behaviour of reinforced concrete rectangular beam specimens with or without FRP-strip shear reinforcement, Adv Eng Softw 67 (2014) 47–56, http://dx.doi.org/10.1016/j.advengsoft.2013.08.001.

[63] A. Godat, K.W. Neale, P. Labossière, Numerical modeling of FRP shear-strengthened reinforced concrete beams, J Compos Constr 11 (6) (2007) 640–649, http://dx.doi.org/10.1061/(ASCE)1090-0268(2007) 11:6(640).

[64] H.-T. Hu, F.-M. Lin, Y.-Y. Jan, Nonlinear finite element analysis of reinforced concrete beams strengthened by fiber-reinforced plastics, Compos Struct 63 (3–4) (2004) 271–281, http://dx.doi.org/10.1016/S0263-8223(03)00174-0.

[65] M. Breveglieri, J.A.O. Barros, G.M. Dalfré, A. Aprile, A parametric study on the effectiveness of the NSM technique for the flexural strengthening of continuous RC slabs, Compos Part B Eng 43 (4) (2012) 1970–1987, http://dx.doi.org/10.1016/j.compositesb.2012.02.008.

[66] V. Bianco, J.A.O. Barros, G. Monti, New approach for modeling the contribution of NSM FRP strips for shear strengthening of RC beams, J Compos Constr 14 (1) (2010) 36–48, http://dx.doi.org/10.1061/(ASCE)CC.1943-5614.0000048.

[67] A. Godat, A. L'Hady, O. Chaallal, K. Neale, Bond behavior of the ETS FRP bar shear-strengthening method, J Compos Constr 16 (5) (2012) 529–530, http://dx.doi.org/10.1061/(ASCE)CC.1943-5614.0000280.

[68] ASCE-ACI Committee 445 on Shear and Torsion, Recent approaches to shear design of structural concrete, J Struct Eng 124 (12) (1998) http://dx.doi.org/10.1061/(ASCE)0733-9445(1998) 124:12(1375.

[69] J.C. Walraven, Fundamental analysis of aggregate interlock, J Struct Div 107 (11) (1981) 2245–2270.

[70] W. Kolmar, Beschreibung der kraftuebertragung über risse in nichtlinearen finite-element-berechnungen von stahlbetontragwerken, Dissertation Darmstadt University of Technology, Germany, 1986.

[71] European Committee for Standardization. Eurocode 2: design of concrete structures – Part 1–1: General rules and rules for buildings Eurocode; 2004.

[72] M. Breveglieri, Shear strengthening of RC beams using the embedded through section technique, Ph.D. Thesis Department of Engineering, Univesity of Ferrara, 2015.